

The authors are grateful to the editor for her time and energy in providing helpful comments that have improved the manuscript. In this document, the editor's comments have been addressed point by point. All the comments are shown in black and author responses are shown in blue text. A manuscript with tracking changes is submitted separately.

Specific comments (Line numbers refer to the document with tracked changes):

1. Line 26: Change “contribute” to “contributed”

→ Corrected as suggested.

2. Experiment names: Thanks for responding to the reviewer's comment in relation to experiment names. May I please ask that you replace “from O3LMA experiment” to “from the O3MLA experiment? This change is also required for “from O3S2007 experiment”, “from BASE experiment”, etc. and should be applied consistently throughout the manuscript.

→ We checked throughout the whole manuscript and made the suggested corrections.

3. Line 394: Please remove “the” in the phrase “and the plant-related factors”

→ Corrected as suggested.

4. Line 395/396: change “by the oxidation factor of root and the aerenchyma factor of plant” to “by the oxidation factor for roots and the aerenchyma factor for plants”

→ Corrected as suggested.

5. Line 396: Change “in root” to “in roots”

→ Corrected as suggested.

6. Line 397: Change “determined by the types of plant in wetland” to “determined by the wetland plant types”

→ Corrected as suggested.

7. Line 398/399: Change “ratio of plant root length density” to “ratio of the plant root length density”

→ Corrected as suggested.

8. Line 399: Change “and root cross-sectional area” to “and the root cross-sectional area”

→Corrected as suggested.

9. Line 400: Change “the diffusion factor of methane from plant root to atmosphere” to “a plant root to atmosphere diffusion factor for methane”

→Corrected as suggested.

10. Line 401: Change “plant species” to “plant type”

→Corrected as suggested.

11. Line 453/454: Change “adopted from the simulations with a chemical transport model used in our previous study” to “adopted from the chemical transport model simulations used in our previous study”

→Corrected as suggested.

12. Line 484: Change “201 sites at the FLUXNET network” to “201 sites from the FLUXNET network”

→Corrected as suggested.

13. Line 484/485: Change “Among these sites, 95 are tree species with the major PFT of ENF” to “Among these sites, 95 have the ENF tree species as the major PFT”

→Corrected as suggested.

14. Line 485: Change “106 are non-tree species with the maximum number for shrubland” to “106 are dominated by shrubland”

→Since the rest 106 sites are not all shrubland, we corrected the sentence as follows: “106 are dominated by non-tree species especially shrubland”.

15. Line 486: Change “of sites” to “of the sites”

→Corrected as suggested.

16. Line 488: Change “to the earlier evaluations” to “to the previous evaluation”

→Corrected as suggested.

17. Line 489: Change “and Southern” to “and in the Southern”

→Corrected as suggested.

18. Line 520-521: Change “Compared to previous evaluations from the YIBs model,

(YU2015),” to “Compared to the previous evaluation of the YIBs model (YU2015),”

→Corrected as suggested.

19. Line 524: Change “cause of such deficit” to “cause of this degradation”

→Corrected as suggested.

20. Line 551: Change “simulations present CH<sub>4</sub> flux” to “simulations give a CH<sub>4</sub> flux”

→Corrected as suggested.

21. Table S1 seems to be missing!

→The updated Table S1 is shown in the revised SI material.

22. Line 161: Replace “grid” with “gridbox”

→Corrected as suggested.

23. Line 214: Change “wetted” to “wet”

→Corrected as suggested.

24. Line 216: Change “is bulk leaf boundary resistance” to “is the bulk leaf boundary resistance”

→Corrected as suggested.

25. Line 734: Change “Meanwhile, iMAPLE model” to “Meanwhile, the iMAPLE model”

→Corrected as suggested.

26. Line 735: Change “at 2-m level” to “down to the 2-m level”

→Corrected as suggested.

27. Line 736/737: Change “may influence the deeper soil interactions between climate and land terrestrial ecosystem especially for the drier conditions.” To “may affect the interactions between climate and the land terrestrial ecosystem especially during drier conditions.”

→Corrected as suggested.

28. Line 327/328: Change “the feedbacks of fire activities on terrestrial ecosystems” to

“the feedbacks from fire activities onto the terrestrial ecosystem”

→Corrected as suggested.

29. Line 328: When referring to iMAPLE, may I please ask that you use “the iMAPLE model” or just “iMAPLE” and not “iMAPLE model” as used here? May I also please ask that make this change consistently throughout the manuscript?

→ We checked throughout the whole manuscript and made the suggested corrections.

30. My understanding from your response to the reviewer’s comment about the complexity of original equation 20 (now equation 25) was that you were going to include a new figure. But Figure R1 seems to be missing!

→We have put Figure R1 into SI as Figure S1. In the main text, we also added the following statement to refer to Figure S1: “The dependence of BAsingle on U and RH is shown in Figure S1.”

31. Line 313: Remove the term “factor”

→Corrected as suggested.

32. Line 460: Change “driven with cycled forcing at the year 1980” to “driven with perpetual forcing for the year 1980”

→Corrected as suggested.

33. Line 477: Change “with the random forest model” to “with a random forest model”

→Corrected as suggested.

34. Line 333: Change “from Coupled Model Intercomparison Project phase 6” to “from Phase 6 of the Coupled Model Intercomparison Project”

→Corrected as suggested.

35. Line 529: Change “and 1°×1° grid” to “and the 1°×1° grid”

→Corrected as suggested.

1 **Development and evaluation of the interactive Model for Air Pollution and Land**  
2 **Ecosystems (iMAPLE) version 1.0**

3  
4 Xu Yue<sup>1#</sup>, Hao Zhou<sup>2,3#</sup>, Chenguang Tian<sup>1</sup>, Yimian Ma<sup>4</sup>, Yihan Hu<sup>1</sup>, Cheng Gong<sup>4</sup>,  
5 Hui Zheng<sup>5</sup>, Hong Liao<sup>1</sup>

6  
7 <sup>1</sup>Jiangsu Key Laboratory of Atmospheric Environment Monitoring and Pollution  
8 Control, Collaborative Innovation Center of Atmospheric Environment and  
9 Equipment Technology, School of Environmental Science and Engineering, Nanjing  
10 University of Information Science & Technology (NUIST), Nanjing, 210044, China

11 <sup>2</sup>College of Meteorology and Oceanography, National University of Defense  
12 Technology, Changsha, 410073, China

13 <sup>3</sup>High Impact Weather Key Laboratory of China Meteorological Administration  
14 (CMA), Changsha, 410073, China

15 <sup>4</sup> Department Biogeochemical Integration, Max Planck Institute for Biogeochemistry,  
16 Jena, 07745, Germany

17 <sup>5</sup> Key Laboratory of Regional Climate-Environment Research for Temperate East  
18 Asia, Institute of Atmospheric Physics, Chinese Academy of Sciences, Beijing,  
19 100029, China

20  
21

22 Corresponding authors: Xu Yue ([yuexu@nuist.edu.cn](mailto:yuexu@nuist.edu.cn))

23  
24

25 # These authors contributed equally

26

## Abstract

Land ecosystems are important sources and sinks of atmospheric components. In turn, air pollutants affect the exchange rates of carbon and water fluxes between ecosystems and atmosphere. However, these biogeochemical processes are usually not well presented in the Earth system models, limiting the explorations of interactions between land ecosystems and air pollutants from the regional to global scales. Here, we develop and validate the interactive Model for Air Pollution and Land Ecosystems (iMAPLE) by upgrading the Yale Interactive terrestrial Biosphere model with process-based water cycles, fire emissions, wetland methane (CH<sub>4</sub>) emissions, and the trait-based ozone (O<sub>3</sub>) damages. Within the iMAPLE, soil moisture and temperature are dynamically calculated based on the water and energy balance in soil layers. Fire emissions are dependent on dryness, lightning, population, and fuel load. Wetland CH<sub>4</sub> is produced but consumed through oxidation, ebullition, diffusion, and plant-mediated transport. The trait-based scheme unifies O<sub>3</sub> sensitivity of different plant functional types (PFTs) with the leaf mass per area. Validations show correlation coefficients (*R*) of 0.59-0.86 for gross primary productivity (GPP) and 0.57-0.84 for evapotranspiration (ET) across the six PFTs at 201 flux tower sites, and yield an average *R* of 0.68 for CH<sub>4</sub> emissions at 44 sites. Simulated soil moisture and temperature match reanalysis data with the high *R* above 0.86 and low normalized mean biases (NMB) within 7%, leading to reasonable simulations of global GPP (*R*=0.92, NMB=1.3%) and ET (*R*=0.93, NMB=-10.4%) against satellite-based observations for 2001-2013. The model predicts an annual global area burned of 507.1 Mha, close to the observations of 475.4 Mha with a spatial *R* of 0.66 for 1997-2016. The wetland CH<sub>4</sub> emissions are estimated to be 153.45 Tg [CH<sub>4</sub>] yr<sup>-1</sup> during 2000-2014, close to the multi-model mean of 148 Tg [CH<sub>4</sub>] yr<sup>-1</sup>. The model also shows reasonable responses of GPP and ET to the changes in diffuse radiation, and yields a mean O<sub>3</sub> damage of 2.9% to global GPP. The iMAPLE [model](#) provides an advanced tool for studying the interactions between land ecosystem and air pollutants.

**Keywords:** carbon fluxes, water cycle, fire emissions, methane emissions, ozone

57 damage, diffuse radiation.

58 **1. Introduction**

59 As an important component on the Earth, land ecosystems regulate global carbon and  
60 water cycles. Every year, the terrestrial ecosystem assimilates ~120 Pg (1 Pg =  $10^{15}$  g)  
61 carbon from atmosphere through vegetation photosynthesis (Beer et al., 2010).  
62 However, most of this carbon uptake returns to atmosphere due to plant and soil  
63 respiration (Sitch et al., 2015), as well as other perturbations such as biomass burning  
64 and biogenic emissions (van der Werf et al., 2010; Carslaw et al., 2010), leading to a  
65 net carbon sink of only ~2 Pg C yr<sup>-1</sup> during 1960-2021 (Friedlingstein et al., 2022).  
66 Meanwhile, land ecosystems affect atmospheric moisture and soil wetness through  
67 both physical (e.g., evaporation and runoff) and physiological (e.g., leaf transpiration  
68 and root hydrological uptake) processes. Observations show that transpiration  
69 accounts for 80%-90% of the terrestrial evapotranspiration (ET) (Jasechko et al., 2013)  
70 and makes significant contributions to land precipitation especially over the tropical  
71 forests (Spracklen et al., 2012).

72

73 Different approaches have been applied to depict the spatiotemporal variations of  
74 ecosystem processes. The eddy covariance technique provides direct measurements of  
75 land carbon and water fluxes (Jung et al., 2011). However, the limited number and  
76 uneven distribution of ground sites results in large uncertainties in the upscaling of  
77 site-level fluxes to the global scale (Jung et al., 2020b). Satellite retrieval provides a  
78 unique tool for the continuous representations of land fluxes in both space and time  
79 (Worden et al., 2021). However, most of the ecosystem variables (e.g., gross primary  
80 productivity, GPP) can only be derived using available signals from remote sensing  
81 through empirical relationships (Madani et al., 2017). As a comparison, process-based  
82 models build physical parameterizations based on field and/or laboratory experiments  
83 and validate against the available *in situ* and satellite-based observations (Niu et al.,  
84 2011; Castillo et al., 2012). These models can be further applied at different spatial  
85 (from site to global) and temporal (from days to centuries) scales to identify the main  
86 drivers of the changes in carbon and water fluxes (Sitch et al., 2015). For example, a



87 total of 17 vegetation models were validated and combined to predict the land carbon  
88 fluxes in the past century (Friedlingstein et al., 2022); the ensemble mean of these  
89 models revealed a steadily increasing land carbon sink from 1960 with the dominant  
90 contribution by CO<sub>2</sub> fertilization.

91

92 While many studies quantified the ecosystem responses to the effects of CO<sub>2</sub>, climate,  
93 and human activities (Piao et al., 2009;Sitch et al., 2015), few have explored the  
94 interactions between air pollution and land ecosystems. Such biogeochemical  
95 processes become increasingly important in the Anthropocene period with significant  
96 changes in atmospheric compositions. For example, observations found that nitrogen  
97 and phosphorus constrain the CO<sub>2</sub> fertilization efficiency of global vegetation (Terrer  
98 et al., 2019), but such limiting effect is ignored or underestimated in most of the  
99 current models (Wang et al., 2020). Tropospheric ozone (O<sub>3</sub>) damages plant  
100 photosynthesis and stomatal conductance, inhibiting carbon assimilation and the ET  
101 from the land surface (Sitch et al., 2007;Lombardozzi et al., 2015). Atmospheric  
102 aerosols can enhance photosynthesis through diffuse fertilization effects (Mercado et  
103 al., 2009) but meanwhile decrease photosynthesis by reducing precipitation (Yue et al.,  
104 2017). In turn, ecosystems act as both the sources and sinks of atmospheric  
105 components. Biomass burning emits a large amount of carbon dioxide, trace gases,  
106 and particulate matter, further influencing air quality (Chen et al., 2021), ecosystem  
107 functions (Yue and Unger, 2018), and global climate (Tian et al., 2022). Biogenic  
108 volatile organic compounds (BVOCs) are important precursors for both surface O<sub>3</sub>  
109 and secondary organic aerosols (Wu et al., 2020), which can feed back to affect  
110 biogenic emissions (Yuan et al., 2016) and carbon assimilation (Rap et al., 2018).  
111 Wetland methane (CH<sub>4</sub>) emissions account for the dominant fraction of natural  
112 sources of CH<sub>4</sub>, and are projected to increase under the global warming scenarios  
113 (Rosentreter et al., 2021;Zhang et al., 2017). On the other hand, stomatal uptake  
114 dominates the dry deposition of air pollutants over the vegetated land (Lin et al.,  
115 2020). Meanwhile, ET from forest results in the increase of water vapor in

116 atmosphere (Spracklen et al., 2012), affecting the consequent rainfall and wet  
117 deposition of particles.

118

119 Currently, numerical models are in general developed separately for atmospheric  
120 chemistry and ecosystem processes. The chemical transport models are usually driven  
121 with prescribed emissions of biomass burning (Warneke et al., 2023) and wetland  
122 methane (Heimann et al., 2020), while the ecosystem models often ignore the  
123 biogeochemical impacts of O<sub>3</sub> and aerosols (Friedlingstein et al., 2022). In an earlier  
124 study, we developed and validated the Yale Interactive terrestrial Biosphere (YIBs)  
125 model version 1.0 with the special focus on the interactions between atmospheric  
126 chemistry and land ecosystems (Yue and Unger, 2015). Thereafter, the YIBs model  
127 has been used offline to assess the O<sub>3</sub> vegetation damage (Yue et al., 2016), aerosol  
128 diffuse fertilization (Yue and Unger, 2017), BVOC emissions (Cao et al., 2021a), as  
129 well as coupled to other models to investigate the carbon-chemistry-climate  
130 interactions (Lei et al., 2020;Gong et al., 2021). The YIBs model has joined the multi-  
131 model intercomparison project of TRENDY since the year 2020 and showed  
132 reasonable performance in the simulation of carbon fluxes (Friedlingstein et al., 2020).  
133 However, the YIBs model failed to predict the typical hydrological variables such as  
134 ET and runoff due to the missing of carbon-water coupling modules. Furthermore, the  
135 model did not consider the nutrient limitation on plant photosynthesis and ignored  
136 some key exchange fluxes between land and atmosphere.

137

138 In this study, we develop the interactive Model for Air Pollution and Land Ecosystems  
139 (iMAPLE) by coupling the process-based water cycle module from Noah-MP (Niu et  
140 al., 2011) to the carbon cycle in the YIBs (Figure 1). In addition, we update the  
141 original YIBs model with some major advances in the biogeochemical processes  
142 including dynamic fire emissions, wetland CH<sub>4</sub> emissions, nutrient limitations on  
143 photosynthesis, and the trait-based O<sub>3</sub> vegetation damage. The detailed descriptions of  
144 these updates are presented in the next section. The iMAPLE [model](#) is fully validated

145 against available measurements in Section 3. The last section will summarize the  
146 model performance and rethink the prospective directions for future development.

147

## 148 **2. Models and data**

### 149 **2.1 Main features of YIBs model**

150 The YIBs model is a process-based vegetation model predicting land carbon fluxes  
151 with dynamic changes in tree height, leaf area index, and carbon pools (Yue and  
152 Unger, 2015, thereafter YU2015). A total of nine plant functional types (PFTs) are  
153 considered including evergreen broadleaf forest (EBF), evergreen needleleaf forest  
154 (ENF), deciduous broadleaf forest (DBF), tundra, shrubland, C<sub>3</sub>/C<sub>4</sub> grassland, and  
155 C<sub>3</sub>/C<sub>4</sub> cropland. At each gridbox, a mixture of PFTs with each PFT fraction is used as  
156 model input, sharing the temperature or moisture information from the same soil  
157 column. Leaf photosynthesis is calculated using the well-established Michaelis-  
158 Menten enzyme-kinetics scheme (Farquhar et al., 1980) and is coupled to stomatal  
159 conductance with the modulations of air humidity and CO<sub>2</sub> concentrations (Ball et al.,  
160 1987). The model applies a two-leaf approach to distinguish the irradiating states for  
161 sunlit and shading leaves and adopts an adaptive stratification for the radiative  
162 transfer processes within canopy layers (Spitters, 1986). The gross carbon  
163 assimilation is further regulated by the optimized plant phenology, which is mainly  
164 dependent on temperature and light for deciduous trees (Yue et al., 2015) but  
165 temperature and/or moisture for shrubland and grassland (YU2015). The assimilated  
166 carbon is allocated among leaf, stem, and root to support autotrophic respiration and  
167 development, the latter of which is used to update plant height and leaf area (Cox,  
168 2001). The input of litterfall triggers the carbon transition among 12 soil carbon pools  
169 and determines the magnitude of heterotrophic respiration with the joint effects of soil  
170 temperature, moisture, and texture (Schaefer et al., 2008). The net carbon uptake is  
171 then calculated by subtracting ecosystem respiration (plant and soil) and  
172 environmental perturbations (reforestation or deforestation) from the gross carbon  
173 assimilation (Yue et al., 2021). The YIBs model reasonably reproduces the observed

174 spatiotemporal patterns of global carbon fluxes and makes contributions to the Global  
 175 Carbon Project with the long-term simulations of land carbon sink in the past century  
 176 (Friedlingstein et al., 2020). The model specifically considers air pollution impacts on  
 177 land ecosystems (Figure 1), such as the ozone vegetation damage (Yue and Unger,  
 178 2014) and aerosol diffuse fertilization effect (Yue and Unger, 2017). The YIBs  
 179 implements two different schemes for BVOCs emissions (Figure 1), including the  
 180 Model of Emissions of Gases and Aerosols from Nature (MEGAN, Guenther et al.,  
 181 2012) and the photosynthesis-dependent (PS\_BVOC) scheme (Unger et al., 2013).

182

## 183 **2.2 New processes in the iMAPLE model**

### 184 2.2.1 Process-based water cycles

185 The descriptions and units of all parameters used in this study are shown in Table S1.  
 186 We implement the hydrological module from Noah-MP into the iMAPLE model (Niu  
 187 et al., 2011). The water budget closure is achieved by constructing water-balance  
 188 equations among precipitation ( $P$ ,  $\text{Kg m}^{-2} \text{s}^{-1}$ ), evapotranspiration ( $ET$ ,  $\text{Kg m}^{-2} \text{s}^{-1}$ ),  
 189 runoff, and terrestrial water storage change ( $\Delta TWS$ ) on each grid cell as follows:

$$190 \quad P = ET + runoff + \Delta TWS \quad (1)$$

191 Here, hourly  $P$  from MERRA-2 reanalyses is used as the input.

192

193 We then divide  $ET$  into three portions including plant transpiration ( $TRA$ ), canopy  
 194 evaporation ( $ECAN$ ) and ground evaporation ( $EGRO$ ):

$$195 \quad ET = TRA + ECAN + EGRO \quad (2)$$

196 For vegetated grids,  $TRA$  is calculated as follows:

$$197 \quad TRA = \frac{\rho_{air} \cdot CP_{air} \cdot C_{tra} \cdot (e_{sat} - e_{ca})}{PC} \quad (3)$$

198 where  $\rho_{air}$  is air density,  $CP_{air}$  is heat capacity of dry air, and  $PC$  is the psychrometric  
 199 constant.  $e_{sat}$  is the saturated vapor pressure at the leaf temperature,  $e_{ca}$  is the vapor  
 200 pressure of the canopy air and  $C_{tra}$  is leaf transpiration conductance, which is  
 201 calculated based on the Ball-Berry scheme of stomatal resistance (Yue and Unger,  
 202 2015). Meanwhile,  $ECAN$  is calculated as follows:

203 
$$ECAN = \frac{\rho_{air} \cdot CP_{air} \cdot C_{canopy, evap} \cdot (e_{sat} - e_{ca})}{PC} \quad (4)$$

204 
$$C_{canopy, evap} = \frac{f_{wet} \cdot E_{VAI}}{R_{leaf, bdy}} \quad (5)$$

205 Here,  $C_{canopy, evap}$  is the latent heat conductance from the wet leaf surface to canopy  
 206 air.  $f_{wet}$  is the wetted fraction of canopy, which is a fraction of the maximum canopy  
 207 precipitation interception capacity.  $E_{VAI}$  is the effective vegetation area index and  
 208  $R_{leaf, bdy}$  is the bulk leaf boundary resistance.  $EGRO$  is calculated as follows:

209 
$$EGRO = C_{ground, evap} (e_{sat, ground} RH - e_{ca}) \quad (6)$$

210 Here,  $C_{ground, evap}$  is the coefficient for latent heat at the ground,  $e_{sat, ground}$  is the  
 211 saturated vapor pressure at the ground and  $RH$  is the surface relative humidity.

212

213 Runoff includes surface ( $R_{srf}$ ) and subsurface ( $R_{sub}$ ) components:

214 
$$runoff = R_{srf} + R_{sub} \quad (7)$$

215 The surface runoff is calculated as follows:

216 
$$R_{srf} = Q_{soil, srf} - Q_{soil, in} \quad (8)$$

217 where  $Q_{soil, srf}$  is the incident water in the soil surface and is the sum of the  
 218 precipitation, snowmelt and dewfall.  $Q_{soil, in}$  is the infiltration into the soil, which is  
 219 derived from approximate solutions of Richards equations with considerations of the  
 220 spatial variations in precipitation and infiltration capacity. Here, we assume  
 221 exponential distributions of infiltration capacity in each grid cell following the  
 222 approach by Schaake et al. (1996):

223 
$$Q_{soil, in} = Q_{soil, srf} \frac{I_c}{Q_{soil, srf} \Delta t + I_c} \quad (9)$$

224 
$$I_c = W_d [1 - \exp(-K_{\Delta t} \Delta t)] \quad (10)$$

225 Here,  $I_c$  and  $W_d$  are the soil infiltration capacity of the model grid cell and the water  
 226 deficit of the soil column, respectively.  $K_{\Delta t}$  and  $\Delta t$  are the calibratable parameters and  
 227 model time step. We assume free drainage processes in the soil column bottom, thus  
 228 the  $R_{sub}$  is calculated as follows:

229 
$$R_{sub} = \alpha_{slope} \cdot K_4 \quad (11)$$

230 where  $\alpha_{slope} = 0.1$  is the terrain slope index.  $K_4$  is the hydraulic conductivity in the

231 bottom soil layer parameterized following the scheme in Clapp and Hornberger (1978)  
 232 and is calculated using spatial soil profiles from Hengl et al. (2017).

233

234 Terrestrial water storage ( $TWS$ ) is the sum of groundwater storage ( $W_{gw}$ ), soil water  
 235 content ( $W_{soil}$ ) and snow water equivalent ( $W_{snow}$ ):

$$236 \quad TWS = W_{gw} + W_{snow} + \sum_{i=1}^{N_{soil}} W_{soil} \quad (12)$$

237 Here, the soil module includes four layers ( $N_{soil} = 4$ ) and  $W_{soil}$  is calculated by the  
 238 volumetric water content ( $W_i$ ) as follows:

$$239 \quad W_{soil} = \rho_{wat} \cdot W_i \cdot \Delta Z_i \quad for \ i = 1, 2, 3, 4 \quad (13)$$

240 where water density ( $\rho_{wat}$ ) = 1000 kg m<sup>-3</sup>, and  $\Delta Z_i$  = 0.1, 0.3, 0.6 and 1m,  
 241 respectively. Hourly  $W_i$  depends on variations of soil water diffusion ( $D$ ) and  
 242 hydraulic conductivity ( $K$ ) as follows:

$$243 \quad \frac{\partial W}{\partial t} = \frac{\partial}{\partial z} \left( D \frac{\partial W}{\partial z} \right) + \frac{\partial K}{\partial z} \quad (14)$$

244 Here,  $K$  and  $D$  are calculated following the parameterizations of Clapp-Hornberger  
 245 curves (Clapp and Hornberger, 1978):

$$246 \quad \frac{K}{K_{sat}} = \left( \frac{W}{W_{sat}} \right)^{2b+3} \quad (15)$$

$$247 \quad D = K \cdot \frac{\partial \varphi}{\partial W} \quad (16)$$

$$248 \quad \frac{\varphi}{\varphi_{sat}} = \left( \frac{W}{W_{sat}} \right)^{-b} \quad (17)$$

249 where  $\varphi_{sat}$ ,  $W_{sat}$  and  $K_{sat}$  are saturated soil capillary potential, volumetric water  
 250 content and hydraulic conductivity. Exponent  $b$  is an empirical constant  
 251 depending on soil types. Soil moisture is calculated as the ratio of  $W_s$  to  $W_{sat}$ .

252

253 Soil temperature ( $T_s$ ) is calculated through physical processes as follows:

$$254 \quad \frac{\partial T_s}{\partial t} = \frac{1}{c} \frac{\partial}{\partial z} \left( K_T \frac{\partial T_s}{\partial z} \right) \quad (18)$$

255 Here  $K_T$  is soil specific heat capacity:

$$256 \quad K_T = K_e \cdot (K_s - K_{dry}) + K_{dry} \quad (19)$$

257 where  $K_e$ ,  $K_s$  and  $K_{dry}$  are Kersten values as a function of soil wetness, saturated soil  
 258 heat conductivity and that under dry air conditions (Niu et al., 2011).  $C$  in Equation  
 259 (13) is the specific heat

$$260 \quad C = W_{lip} \cdot C_{lip} + W_{ice} \cdot C_{ice} + (1 - W_{sat}) \cdot C_{sat} + (W_{sat} - W) \cdot C_{air} \quad (20)$$

261 Here,  $W_{lip}$ ,  $C_{lip}$  and  $W_{ice}$ ,  $C_{ice}$  indicate water content and heat capacity on soil water  
 262 and ice.  $C_{sat}$  and  $C_{air}$  are saturated and air heat capacity, which are empirical  
 263 constants (Niu et al., 2011).

264

### 265 2.2.2 Dynamic fire emissions

266 We implement the active global fire parameterizations from Pechony and Shindell  
 267 (2009) and Li et al. (2012) to the iMAPLE model. The fire emissions are determined  
 268 by several key factors such as fuel flammability, natural ignitions, human activities,  
 269 and fire spread. The fire count  $N_{fire}$  depends on flammability ( $Flam$ ), fire ignition  
 270 (including both natural ignition rate  $I_N$  and anthropogenic ignition rate  $I_A$  and  
 271 anthropogenic suppression ( $F_{NS}$ ):

$$272 \quad N_{fire} = Flam \times (I_N + I_A) \times F_{NS} \quad (21)$$

273  $Flam$  is a unitless metric representing conditions conducive to fire occurrence. It is  
 274 parameterized as a function of vapor pressure deficit (VPD), precipitation (Prec), and  
 275 leaf area index (LAI):

$$276 \quad Flam = VPD \times e^{-2 \times Prec} \times LAI \quad (22)$$

277  $I_N$  depends on the cloud-to-ground lightning and  $I_A$  can be expressed as:

$$278 \quad I_A = 0.03 \times PD \times k(PD) \quad (23)$$

279 where  $PD$  is population density. The empirical function of  $k(PD) = 6.8 \times PD^{-0.6}$   
 280 stands for ignition potentials by human activity. The fraction of non-suppressed fires  
 281  $F_{NS}$  is derived as:

$$282 \quad F_{NS} = 0.05 + 0.95 \times e^{-0.05 \times PD} \quad (24)$$

283

284 The burned area of a single fire ( $BA_{single}$ ) is typically taken to be elliptical in shape  
 285 associated with length-to-breadth ratio ( $LB$ ), head-to-back ratio (HB) and rate of fire

286 spread ( $UP$ ) as follows:

$$287 \quad BA_{single} = \frac{\pi \times UP^2}{4 \times LB} \times \left(1 + \frac{1}{HB}\right)^2 \quad (25)$$

288 Then,  $LB$  and  $HB$  are related to changes of near-surface wind speed ( $U$ ) as follows:

$$289 \quad LB = 1 + 10 \times (1 - e^{-0.06 \times U}) \quad (26)$$

$$290 \quad HB = \frac{LB + (LB^2 - 1)^{0.5}}{LB - (LB^2 - 1)^{0.5}} \quad (27)$$

291 Meanwhile,  $UP$  is computed as the function of relative humidity ( $RH$ ):

$$292 \quad UP = UP_{max} \times f_{RH} \times f_{\theta} \times G(W) \quad (28)$$

293 Here,  $UP_{max}$  is the maximum fire spread rate depending on PFTs,  $f_{RH}$  and  $f_{\theta}$  represent  
294 the dependence of fire spread on  $RH$  and on root-zone soil moisture, respectively.  $f_{\theta}$   
295 is simply set to 0.5 and  $f_{RH}$  is calculated as:

$$296 \quad f_{RH} = \begin{cases} 1, & RH \leq RH_{low} \\ \frac{RH - RH_{low}}{RH_{up} - RH_{low}}, & RH_{low} < RH < RH_{up} \\ 0, & RH \geq RH_{up} \end{cases} \quad (29)$$

297 In this study, we set  $RH_{low} = 30\%$  and  $RH_{up} = 70\%$  as the lower and upper thresholds  
298 of  $RH$  following the methods used in Li et al. (2012). If  $RH$  is higher than 70%,  
299 natural fires will not occur or spread, and  $RH$  will no longer be a constraint factor for  
300 fire occurrence and spread if  $RH \leq 30\%$ .  $G(W)$  is the limit of the fire spread:

$$301 \quad G(W) = \frac{LB}{1 + \frac{1}{HB}} \quad (30)$$

302 In general, the eccentricity of burned area is primarily influenced by near-surface  
303 wind speed, while the rate of fire spread is jointly regulated by near-surface wind  
304 speed and relative humidity. The shape of the fire is converted to a circular form when  
305 the near-surface wind speed reaches zero, and burning ceases to propagate once the  
306 relative humidity is above a specific threshold. The dependence of  $BA_{single}$  on  $U$  and  
307  $RH$  is shown in Figure S1.

309 Finally, the burned area ( $BA$ ) is represented as:

$$310 \quad BA = BA_{single} \times N_{fire} \quad (31)$$

311 The fire-emitted trace gases and aerosols ( $Emis$ ) are calculated as:

$$312 \quad Emis = BA \times EF \quad (32)$$

Formatted: Font: Italic

Formatted: Font: Italic

Formatted: Font: Italic

Formatted: Font: Italic

Formatted: Font: Italic, Subscript

Formatted: Font: Italic

Formatted: Font: Italic



313 where  $EF$  is the emission factors for different species (such as black carbon and  
 314 organic carbon aerosols). It is important to note that the feedbacks ~~of~~-from fire  
 315 activities onto the terrestrial ecosystems have not been considered in the current  
 316 version of the iMAPLE model due to the high complexity.

317

### 318 2.2.3 Wetland methane emissions

319 We implement the process-based wetland  $CH_4$  emissions into the iMAPLE model.  
 320 The anthropogenic sources of  $CH_4$  from Phase 6 of the Coupled Model  
 321 Intercomparison Project ~~phase 6~~ (CMIP6, [https://esgf-](https://esgf-node.llnl.gov/projects/input4mips/)  
 322 [node.llnl.gov/projects/input4mips/](https://esgf-node.llnl.gov/projects/input4mips/)) are also used as input for iMAPLE. For each soil  
 323 layer, the flux of  $CH_4$  ( $F_{CH_4}$ ) is calculated as the difference between production ( $P_{CH_4}$ )  
 324 and consumptions, which include oxidation ( $O_{CH_4}$ ), ebullition ( $E_{CH_4}$ ), diffusion ( $D_{CH_4}$ ),  
 325 and plant-mediated transport through aerenchyma ( $A_{CH_4}$ ) as follows:

$$326 \quad F_{CH_4} = P_{CH_4} - O_{CH_4} - E_{CH_4} - D_{CH_4} - A_{CH_4} \quad (33)$$

327 The net methane emission to the atmosphere is the sum of ebullition, diffusion and  
 328 aerenchyma transport from the top soil layer.

329

330 The production of  $CH_4$  in soil depends on the quantity of carbon substrate and  
 331 environmental conditions including soil temperature  $T_s$ , pH, and wetland inundation  
 332 fraction  $f_{wetland}$  as follows:

$$333 \quad P_{CH_4} = R_h r f_{T_s} f_{pH} f_{wetland} \quad (34)$$

334 where  $R_h$  is the heterotrophic respiration estimated at the grid cell ( $mol\ C\ m^{-2}\ s^{-1}$ ).  
 335  $r$  represents the release ratio of methane and carbon dioxide (Wania et al., 2010). We  
 336 determine the dependence on  $T_s$  and soil pH in iMAPLE based on the  
 337 parameterizations from the TRIPLEX-GHG model (Zhu et al., 2014). The impact  
 338 factor of soil temperature  $f_{ST}$  can be calculated as follows (Zhang et al., 2002; Zhu et  
 339 al., 2014):

$$340 \quad f_{ST} = \begin{cases} 0, & T_s < T_{min} \\ vt^{xt} \exp(xt(1 - vt)), & T_{min} \leq T_s \leq T_{max} \\ 0, & T_s > T_{max} \end{cases} \quad (35)$$

341 
$$vt = (T_{max} - T_s)/(T_{max} - T_{opt}) \quad (36)$$

342 
$$xt = [\log(Q_{10})(T_{max} - T_{opt})]^2(1.0 + at^{0.5})^2/400.0 \quad (37)$$

343 
$$at = 1.0 + 40.0/[\log(Q_{10})(T_{max} - T_{opt})] \quad (38)$$

344  $T_{min}$ ,  $T_{max}$ , and  $T_{opt}$  represents the lowest, highest and optimum temperature for the  
 345 process of methane production and oxidation, respectively. In this study, the  $T_{min} =$   
 346  $0^\circ\text{C}$ ,  $T_{max} = 45^\circ\text{C}$  and  $T_{opt} = 25^\circ\text{C}$  (Zhu et al., 2014).

347

348 For the temperature-dependence, the  $Q_{10}$  relationships are applied as follows:

349 
$$Q_{10} = r_b Q_b^{\frac{T_s - T_{base}}{10}} \quad (39)$$

350 Here  $r_b$  is set to 3.0 and  $Q_b$  is 1.33 with a base temperature ( $T_{base}$ ) of  $25^\circ\text{C}$  (Zhu et al.,  
 351 2014;Paudel et al., 2016). The inundation fraction of wetland at each cell describes  
 352 the proportion of anaerobic conditions (Zhang et al., 2021). We ignore the impact of  
 353 redox potential (Eh) because global observations are not available and the Eh-related  
 354 processes are poorly characterized in current models (Wania et al., 2010).

355

356 The oxidation of  $\text{CH}_4$  is a series of aerobic activities related to temperature and  $\text{CH}_4$   
 357 concentrations:

358 
$$O_{CH_4} = [CH_4]f_{Ts}f_{CH_4} \quad (40)$$

359 where  $[CH_4]$  is the methane amount in each soil layer ( $gCm^{-2}layer^{-1}$ ).  $f_{CH_4}$  is the  
 360  $\text{CH}_4$  concentration factor representing a Michaelis-Menten kinetic relationship:

361 
$$f_{CH_4} = \frac{[CH_4]}{[CH_4] + K_{CH_4}} \quad (41)$$

362 where  $K_{CH_4} = 5 \mu\text{mol } L^{-1}$  is the half-saturation coefficient with respect to  $\text{CH}_4$   
 363 (Walter and Heimann, 2000). For temperature-dependence of oxidation, the  $Q_{10}$   
 364 relationship with  $r_b = 2.0$ ,  $Q_b = 1.9$ , and  $T_{base} = 12^\circ\text{C}$  is adopted (Zhu et al.,  
 365 2014;Paudel et al., 2016).

366

367 The diffusion of  $\text{CH}_4$  follows the Fick's law with dependence on  $\text{CH}_4$  concentrations  
 368 and the molecular diffusion coefficients of  $\text{CH}_4$  in the air ( $D_a = 0.2 \text{ cm}^2\text{s}^{-1}$ ) and water



398 Then the down-regulated photosynthesis is calculated by scaling the original value  
 399 with the factor of  $\varepsilon$ .

400

#### 401 2.2.5 Trait-based O<sub>3</sub> vegetation damaging scheme

402 The YIBs model considers O<sub>3</sub> vegetation damage using the flux-based scheme  
 403 proposed by Sitch et al. (2007) (thereafter S2007), which determines the damaging  
 404 ratio  $F$  of plant photosynthesis as follows:

$$405 \quad F = a_{PFT} \times \max\{f_{O_3} - t_{PFT}, 0\} \quad (44)$$

406 Here, the  $f_{O_3}$  denotes O<sub>3</sub> stomatal flux (nmol m<sup>-2</sup> s<sup>-1</sup>) defined as:

$$407 \quad f_{O_3} = \frac{[O_3]}{r + \left[ \frac{k_{O_3}}{g_p \times (1-F)} \right]} \quad (45)$$

408 where  $[O_3]$  represents the O<sub>3</sub> concentrations at the reference level (nmol m<sup>-3</sup>).  $r$  is the  
 409 sum of boundary and aerodynamic resistance between leaf surface and reference level  
 410 (s m<sup>-1</sup>).  $g_p$  is the potential stomatal conductance for H<sub>2</sub>O (m s<sup>-1</sup>).  $k_{O_3} = 1.67$  is a  
 411 conversion factor of leaf resistance for O<sub>3</sub> to that for water vapor. The level of O<sub>3</sub>  
 412 damage is then determined by the PFT-specific sensitivity  $a_{PFT}$  and threshold  $t_{PFT}$ ,  
 413 which are different among PFTs.

414

415 In iMAPLE, we implement the trait-based O<sub>3</sub> vegetation damaging scheme to unify  
 416 the inter-PFT sensitivities (Ma et al., 2023):

$$417 \quad a_{PFT} = \frac{a}{LMA} \quad (46)$$

418 Here, a unified plant sensitivity  $a$  (nmol<sup>-1</sup> g s) is scaled by leaf mass per area (LMA, g  
 419 m<sup>-2</sup>) to derive the sensitivity of a specific PFT ( $a_{PFT}$ ). Accordingly, the damaging  
 420 fraction  $F$  is modified as follows:

$$421 \quad F = a \times \max\left\{ \frac{f_{O_3}}{LMA} - t, 0 \right\} \quad (47)$$

422 Here  $t$  (nmol g<sup>-1</sup> s<sup>-1</sup>) is a unified flux threshold for O<sub>3</sub> vegetation damage. The  $f_{O_3}$  in  
 423 Equation (45) is fed into Equation (47) so as to build a quadratic equation for  $F$ . We  
 424 solve the quadratic equation and select the  $F$  value within the range of [0, 1]. The  
 425 updated scheme considers the dilution effects of O<sub>3</sub> dose through leaf cross-section by

426 incorporating LMA. Plants with high LMA (e.g., ENF and EBF) usually have low  
427 sensitivities, and those with low LMA (e.g., DBF and crops) are more sensitive to O<sub>3</sub>  
428 damages. The unified sensitivity  $a$  is set to 3.5 nmol<sup>-1</sup> g s and threshold  $t$  is set to  
429 0.019 nmol g<sup>-1</sup> s<sup>-1</sup> by calibrating simulated  $F$  values with literature-based  
430 measurements (Ma et al., 2023).

431

### 432 **2.3 Design of simulations**

433 We perform four sensitivity experiments with the iMAPLE model. The baseline  
434 (BASE) simulation considers the two-way coupling between carbon and water cycles,  
435 so that the prognostic soil meteorology drives canopy photosynthesis and  
436 evapotranspiration. A sensitivity run named BASE\_NW is set up by turning off the  
437 water cycle in the iMAPLE model. In this simulation, the soil moisture and soil  
438 temperature are adopted from the Modern-Era Retrospective Analysis for Research  
439 and Applications, Version 2 (MERRA-2) reanalyses (Gelaro et al., 2017). The third  
440 and fourth runs turn on the O<sub>3</sub> vegetation damage effect using either the LMA-based  
441 scheme (O3LMA) or the S2007 scheme (O3S2007). Surface hourly O<sub>3</sub> concentrations  
442 are adopted from the ~~simulations with a~~ chemical transport model ~~simulations~~ used in  
443 our previous study (Yue and Unger, 2018). For all simulations, the iMAPLE model is  
444 driven with the hourly surface meteorology at a spatial resolution of 1°×1° from the  
445 MERRA-2 reanalyses, including surface air temperature, air pressure, specific  
446 humidity, wind speed, precipitation, snowfall, shortwave and longwave radiation. We  
447 run the model for the period of 1980-2021 using the initial conditions of the  
448 equilibrium soil carbon pool, tree height, and water fluxes from a spin-up run of 200  
449 years driven with ~~eyeled-perpetual~~ forcing ~~at-for~~ the year 1980.

450

451 The iMAPLE model is driven with observed CO<sub>2</sub> concentrations from Mauna Loa  
452 (Keeling et al., 1976) and the land cover fraction of nine PFTs derived by combining  
453 satellite retrievals from both Moderate Resolution Imaging Spectroradiometer  
454 (MODIS) (Hansen et al., 2003) and Advanced Very High Resolution Radiometer

455 (AVHRR) (Defries et al., 2000). For fire emissions, we use Gridded Population of the  
456 World version 4 (<https://sedac.ciesin.columbia.edu/data/collection/gpw-v4>) to  
457 calculate human ignition and suppression. The lightning ignition is calculated using  
458 the flash rate from Very High Resolution Gridded Lightning Climatology Data  
459 CollectionVersion1([https://ghrc.nsstc.nasa.gov/uso/ds\\_details/collections/lisvhrcC.ht](https://ghrc.nsstc.nasa.gov/uso/ds_details/collections/lisvhrcC.html)  
460 ml). For wetland CH<sub>4</sub> emissions, we use the 2000-2020 global dataset of Wetland  
461 Area and Dynamics for Methane Modeling (WAD2M) derived from static datasets  
462 and remote sensing (Zhang et al., 2021), global soil pH from Hengl et al. (2017), and  
463 gridded soil texture from Scholes et al. (2011). For the LMA-based O<sub>3</sub> damage  
464 scheme, we use gridded LMA from the trait-level dataset of TRY (Kattge et al., 2011)  
465 developed by extending field measurements with ~~the a~~ random forest model (Moreno-  
466 Martínez et al., 2018).

467

#### 468 **2.4 Data for validations**

469 We use observational datasets to validate the biogeochemical processes and related  
470 variables simulated by the iMAPLE model. For simulated carbon and water fluxes,  
471 site-level observations are collected from 201 sites ~~at-from~~ the FLUXNET network  
472 (Table S2 and Figure 2). Among these sites, 95 ~~are-have the ENF~~ tree species ~~with-as~~  
473 the major PFT ~~of ENF~~ and 106 are ~~dominated by non-tree species with the maximum~~  
474 ~~number for non-tree species especially~~ shrubland. Most (71%) of ~~the~~ sites are located  
475 at the middle latitudes (30°-60°N) of the Northern Hemisphere (NH), especially in the  
476 U.S. and Europe. Compared to the ~~earlier-previous~~ evaluations in YU2015, we have  
477 many more sites in the tropics (22 in this study vs. 5 in YU2015), Asia (20 in this  
478 study vs. 1 in YU2015), and ~~in the~~ Southern Hemisphere (28 in this study vs. 7 in  
479 YU2015) in this study. We also use the global gridded observations of GPP from the  
480 satellite retrievals including the solar-induced chlorophyll fluorescence (SIF) product  
481 GOSIF (Li and Xiao, 2019) and the Global land surface satellite (GLASS) product  
482 (Yuan et al., 2010). The global observations of ET are adopted from the benchmark  
483 product of FLUXCOM (Jung et al., 2020a) and the satellite-based GLASS product.

484 For the dynamic fire module, we use monthly observed area burned from the Global  
485 Fire Emission Database version 4.1 with small fires (GFED4.1s) during 1997-2016  
486 (van der Werf et al., 2010; Randerson et al., 2012). For methane emissions, we use  
487 site-level measurements of CH<sub>4</sub> fluxes from the FLUXNET-CH<sub>4</sub> network (Delwiche  
488 et al., 2021). We exclude the monthly records with missing data at more than half of  
489 the days and calculate the long-term mean fluxes for the seasonal cycle. In total, we  
490 select 44 sites with at least six months of data available for the validations (Table S3).

491

### 492 **3. Model evaluations**

#### 493 3.1 Site-level evaluations

494 Simulated GPP shows correlation coefficients (R) of 0.59-0.86 for the six main PFTs  
495 with varied sample numbers (Figure 3). The highest R is achieved for ENF, though  
496 the model underestimates the mean GPP magnitude by 20.62% for this species. On  
497 average, simulated GPP is lower than observations for most PFTs. Compared to  
498 previous evaluation ~~ofs from~~ the YIBs model (YU2015), iMAPLE with coupled water  
499 cycle improves the R of GPP simulations for ENF (from 0.65 to 0.86) and grassland  
500 (from 0.7 to 0.8) but worsens the predictions for other species such as EBF (from 0.65  
501 to 0.59). The main cause of ~~such this degradation deficit~~ is the application of MERRA-  
502 2 reanalyses in the iMAPLE simulations instead of the site-level meteorology used in  
503 the YU2015. The biases in the meteorological input may cause uncertainties in the  
504 simulation of GPP fluxes (Ma et al., 2021). In addition, the mismatch of vegetation  
505 cover and soil properties between the site location and ~~the~~ 1°×1° grid in the simulation  
506 may further contribute to the modeling biases.

507

508 Simulated ET matches observations with correlation coefficients of 0.57-0.84 at the  
509 FLUXNET sites (Figure 4). Relatively better performance is achieved for ENF  
510 (R=0.83) and grassland (R=0.84), for which the model yields good predictions of GPP  
511 as well. In contrast, low correlations and high biases are predicted for shrubland and  
512 cropland. For the shrubland sites, different land types (e.g., closed shrublands,

513 permanent wetlands, and woody savannas) share the same parameters in the iMAPLE  
514 model, resulting in the biases in depicting the site-specific carbon and water fluxes.  
515 For cropland, the prognostic phenology of grass species is applied in the model due to  
516 the missing of plantation information for individual sites. Even with these deficits, the  
517 iMAPLE model in general captures the spatiotemporal variations of GPP and ET at  
518 most sites.

519

520 We further compare the simulated wetland CH<sub>4</sub> fluxes from [the](#) BASE experiment  
521 with observations at the FLUXNET-CH<sub>4</sub> sites. Similar to the carbon flux sites, most  
522 of these CH<sub>4</sub> flux sites are located in the NH (Figure 5a). However, different from the  
523 carbon fluxes which usually range from 0 to 15 g C m<sup>-2</sup> day<sup>-1</sup>, the CH<sub>4</sub> fluxes show a  
524 wide range across several orders of magnitude from 10<sup>-2</sup> to 10<sup>3</sup> g [CH<sub>4</sub>] m<sup>-2</sup> yr<sup>-1</sup>  
525 (Figure 5b). Such a large contrast requires a more realistic configuration of model  
526 parameters to distinguish the large gradient among sites. For example, US-Tw1 and  
527 US-Tw4 are two nearby sites within a distance of 1 km, where our simulations [present](#)  
528 [give a](#) CH<sub>4</sub> flux of 14.35 g[CH<sub>4</sub>] m<sup>-2</sup> yr<sup>-1</sup> during 2011-2017. However, average CH<sub>4</sub>  
529 flux shows a difference of 3.7 times with 66.31 g[CH<sub>4</sub>] m<sup>-2</sup> yr<sup>-1</sup> in US-Tw1 and 18.16  
530 g[CH<sub>4</sub>] m<sup>-2</sup> yr<sup>-1</sup> in US-Tw4 during 2011-2017. In the model, these two sites share the  
531 same land surface properties because they are located on the same grid. On average,  
532 simulated CH<sub>4</sub> fluxes are correlated with observations at a moderate R of 0.68 and a  
533 normalized mean bias (NMB) of -28%.

534

### 535 3.2 Grid-level evaluations

536 The coupling of Noah-MP module enables the dynamic prediction of soil parameters  
537 by the iMAPLE model. We compare the simulated soil moisture and soil temperature  
538 from [the](#) BASE experiment with MERRA-2 reanalyses (Figure 6). Both simulations  
539 (Figure 6a) and observations (Figure 6b) show low soil moisture over arid and semi-  
540 arid regions with the minimum in North Africa. The model also captures the high soil  
541 moisture in tropical rainforest. However, the prediction underestimates soil moisture



542 in boreal regions in NH (Figure 6c). On the global scale, simulated soil moisture  
543 matches observations with a high R of 0.86 and a low NMB of -6.9%. These  
544 statistical metrics are further improved for the simulated soil temperature with the R  
545 of 0.99 and NMB of 0.5% against observations (Figure 6f). The simulation  
546 reproduces the observed spatial pattern with a uniform warming bias.

547

548 Driven with the prognostic soil moisture and temperature, the iMAPLE model  
549 predicts reasonable land carbon and water fluxes (Figure 7). Simulated GPP (Figure  
550 7a) reproduces observed patterns (Figure 7b) with high values in the tropical  
551 rainforest, moderate values in the boreal forests, and low values in the arid regions.  
552 On the global scale, our simulations yield a total GPP of 129.8 Pg C yr<sup>-1</sup>, similar to  
553 the observed amount of 125.4 Pg C yr<sup>-1</sup>. The predicted GPP is higher than  
554 observations over the tropical rainforest (Figure 7c). However, such overestimation  
555 may instead be an indicator of biases in the ensemble observations, which are derived  
556 from the empirical models instead of direct measurements (Yuan et al., 2010;Running  
557 et al., 2004). Our site-level evaluations show that iMAPLE predicts reasonable GPP  
558 values at the EBF sites (Figure 3). Despite this inconsistency, the model yields a high  
559 R of 0.92 and a small NMB of 1.3% for GPP against observations on the global scale  
560 (Figure 7c). Simulated ET (Figure 7d) matches the observations (Figure 7e) with high  
561 values in the tropical rainforest and secondary high values in the boreal forest. In  
562 general, the prediction is lower than observations except for the eastern U.S. and  
563 eastern China (Figure 7f). On average, the iMAPLE model shows the R of 0.93 and  
564 NMB of -10.4% in the simulation of ET compared to the ensemble of observations.

565

566 We further compare the simulated GPP with (BASE) or without (BASE\_NW)  
567 dynamic water cycle (Figure 8). Relative to the simulations driven with MERRA-2  
568 soil moisture and temperature, the iMAPLE model coupled with Noah-MP water  
569 module predicts very similar GPP over the hotspot regions such as tropical rainforest  
570 and boreal forest (Figure 8a). However, the coupled model predicts lower GPP for

571 grassland in the tropics (e.g., South America and central Africa) but higher GPP in  
572 arid regions (e.g., South Africa and Australia). Since the baseline GPP is very low in  
573 arid regions, the relative changes are even larger than 100% over those areas. These  
574 GPP differences are mainly driven by the changes in soil moisture, which increases  
575 over the arid regions with the dynamic water cycle (Figure 6c). The reduction of soil  
576 moisture in the high latitudes of NH shows limited impacts on the predicted GPP,  
577 likely because the boreal ecosystem is more dependent on temperature than moisture  
578 (Beer et al., 2010).

579

### 580 3.3 Ecosystem perturbations to air pollution

581 Within the iMAPLE framework, the land ecosystem perturbs atmospheric  
582 components through the emissions from biomass burning, wetland CH<sub>4</sub>, and BVOCs.  
583 We compare the simulated burned fraction and fire-emitted organic carbon (OC)  
584 emissions with observations from GFED4.1s (Figure 9). The largest burned fraction is  
585 predicted over the Sahel region and countries of Angola and Zambia, surrounding the  
586 low center of Congo rainforest. Moderate burnings could be found in northern  
587 Australia and eastern South America. Most of these hotspots are located on the  
588 grassland and shrubland in the tropics, where the high temperature and limited rainfall  
589 promotes regional fire activities. The model reasonably captures the observed fire  
590 pattern with a spatial correlation of 0.66 and NMB of 6.05% (Figure 9c), though the  
591 model overestimates the area burned in South Africa. The predicted fire area is used to  
592 derive biomass burning emissions of air pollutants (e.g., carbon monoxide, nitrogen  
593 oxides, black carbon, organic carbon, sulfur dioxide) with the specific emission  
594 factors (Tian et al., 2023). Furthermore, we compare fire-emitted OC from the model  
595 with GFED4.1s. The spatial pattern of OC emissions is similar to that of burned area.  
596 The simulations yield a total of 16.8 Tg yr<sup>-1</sup> for the global fire-emitted OC, slightly  
597 higher than the amount of 16.4 Tg yr<sup>-1</sup> from GFED4.1s with some overestimations in  
598 tropical Africa (Figure 9f).

599

600 The wetland emissions of CH<sub>4</sub> show hotspots over tropical rainforests (Figure 10a),  
601 where the dense soil carbon provides abundant substrates for emissions and the warm  
602 climate promotes the emission rates. The secondary hotspots are located at the boreal  
603 regions in the NH. This spatial pattern is very similar to the map of wetland CH<sub>4</sub>  
604 emissions predicted by an ensemble of 13 biogeochemical models (Saunois et al.,  
605 2020). On the global scale, the total wetland emission is 153.45 Tg [CH<sub>4</sub>] yr<sup>-1</sup> during  
606 2000-2014, close to the average of 148±25 Tg [CH<sub>4</sub>] yr<sup>-1</sup> for 2000-2017 estimated by  
607 the multiple models. As a comparison, anthropogenic source of CH<sub>4</sub> show the high  
608 amount in China and India due to the large emissions from fossil fuels and agriculture  
609 (Figure 10b). On the global scale, the wetland emissions are equivalent to 45.3% of  
610 the total anthropogenic emissions. As important factors driving CH<sub>4</sub> emissions,  
611 heterotrophic respiration shows higher values over tropical regions and eastern China  
612 with a total amount of 73.2 Pg C yr<sup>-1</sup> (Figure 10c), and relative high wetland  
613 coverages are found in boreal Asia and Amazon (Figure 10d).

614

615 Isoprene emissions from the two schemes in the iMAPLE model show similar spatial  
616 distributions with the hotspots over tropical rainforest (Figure 11), where the warm  
617 climate and abundant light are favorable for the biogenic emissions. Compared to the  
618 MEGAN scheme, the PS\_BVOC scheme yields higher emissions in the tropical  
619 rainforest and boreal forest, but lower emissions for the shrubland and grassland in  
620 semiarid regions (Figure 11c). Such differences are attributed to the varied processes  
621 as well as the emission factors. Our earlier study showed that PS\_BVOC scheme  
622 predicts stronger trends in isoprene emissions than MEGAN (Cao et al., 2021a),  
623 because the former considers both CO<sub>2</sub> fertilization and inhibition effects while the  
624 latter considers only the inhibition effects. On the global scale, isoprene emissions are  
625 550 Tg yr<sup>-1</sup> with PS\_BVOC (Figure 11a) and 611 Tg yr<sup>-1</sup> with MEGAN (Figure 11b).  
626 These amounts are higher than the ensemble mean of 448 Tg yr<sup>-1</sup> from the CMIP6  
627 models (Cao et al., 2021b), but in general within the range of 412-601 Tg yr<sup>-1</sup> as  
628 summarized by Carslaw et al. (2010).

629

#### 630 3.4. Air pollution impacts on ecosystem fluxes

631 We assess the damaging effects of surface O<sub>3</sub> to GPP with two schemes (O3LMA –  
632 BASE and O3S2007 - BASE) (Figure 12). Simulated GPP losses show similar  
633 patterns with high damages in eastern U.S., western Europe, and eastern China, where  
634 surface O<sub>3</sub> level is high due to the anthropogenic emissions. Limited GPP damages  
635 are predicted in the tropics though with abundant forest coverage due to the low level  
636 of O<sub>3</sub> pollution. Compared to the S2007 scheme, predicted GPP loss is further  
637 alleviated in tropical rainforest with the LMA-based scheme, because the latter  
638 scheme determines lower O<sub>3</sub> sensitivity for evergreen trees due to their higher content  
639 of chemical resistance with the larger LMA value (Ma et al., 2023). On the global  
640 scale, the average GPP loss is -2.9% with the LMA scheme and -3.2% with the S2007  
641 scheme. Such damage to GPP is weaker than the estimate of -4.8% in Ma et al. (2023)  
642 because of the differences in O<sub>3</sub> concentrations, vegetation types, and photosynthetic  
643 parameters.

644

645 Atmospheric aerosols cause perturbations to both direct and diffuse radiation, which  
646 have different efficiencies in enhancing plant photosynthesis. Here, we separate the  
647 diffuse (diffuse fraction > 0.75) and direct (diffuse fraction < 0.25) components using  
648 observed diffuse fraction and solar radiation at six FLUXNET sites, and aggregate the  
649 GPP and ET fluxes for different radiation periods at certain intervals (Figure 13). At  
650 the six selected sites, observed GPP is higher and grows faster with more diffusive  
651 light than that under the direct light conditions (Figure 13a-13f). Simulations in  
652 general reproduce such feature with the comparable variability. In the earlier study,  
653 simulated diffuse fertilization efficiency for GPP (changes of GPP per unit diffuse  
654 radiation) was well validated against observations at more than 20 sites (Yue and  
655 Unger, 2018). Such amelioration of GPP suggests that moderate aerosol loading is  
656 beneficial for ecosystem carbon uptake (Yue and Unger, 2017). However, the dense  
657 aerosol loading may instead weaken plant photosynthesis due to the large reduction in

658 direct radiation.

659

660 We further evaluate the ET responses to diffuse and direct radiation from the iMAPLE  
661 model (Figure 13g-13i). Although ET is slightly higher at the diffusive condition, the  
662 growth rates are weaker than that of GPP. The main cause of such difference is related  
663 to the varied light dependence of ET components, which consist of canopy  
664 evaporation and transpiration. Transpiration is tightly coupled with photosynthesis  
665 and will increase by diffuse radiation at a similar rate. However, evaporation is more  
666 dependent on light quantity which will decrease with the extinction of aerosols. As a  
667 result, the weakened evaporation in part offsets the increased transpiration, leading to  
668 the smaller growth rate of ET than the responses of photosynthesis and the consequent  
669 enhancement in water use efficiency (Wang et al., 2023). The iMAPLE model  
670 reasonably captures the lower growth rates of ET than GPP in response to diffuse  
671 radiation at the selected sites.

672

#### 673 **4. Conclusions and discussion**

674 We develop the iMAPLE model by coupling Noah-MP water module with YIBs  
675 vegetation model. Validations show that iMAPLE predicts reasonable distribution of  
676 soil moisture and soil temperature. Driven with these prognostic soil conditions and  
677 meteorology from reanalyses, the model reasonably reproduces the observed  
678 spatiotemporal variations of both GPP and ET fluxes at 201 sites and on the global  
679 scale. We further update the biogeochemical processes in iMAPLE to extend the  
680 model's capability in quantifying interactions between air pollution and land  
681 ecosystems. The model reasonably predicts wetland CH<sub>4</sub> emissions at 44 sites and  
682 yields the similar global map of CH<sub>4</sub> emissions compared to an ensemble of 13  
683 biogeochemical models. In addition, predicted biomass burning and biogenic  
684 emissions are consistent with either satellite retrievals or results from other models.  
685 We assess the impacts of surface O<sub>3</sub> and aerosols on ecosystem fluxes. The LMA-  
686 based scheme links the O<sub>3</sub> sensitivity with vegetation LMA and predicts a global map

687 of GPP loss that is consistent with the traditional scheme using the PFT-specific  
688 sensitivity. The updated scheme effectively reduces modeling uncertainties by  
689 decreasing the number of parameters for O<sub>3</sub> sensitivity and provides an option to  
690 apply the advanced LMA map from remote sensing. The model also reproduces the  
691 observed responses of GPP and ET to diffuse radiation with a lower growth rate for  
692 ET than GPP.

693

694 There are several limitations in the current version of iMAPLE ~~model~~. First, it does  
695 not include the dynamic nutrient cycle. Although we implement the down regulation  
696 from Arora et al. (2009) to constrain CO<sub>2</sub> fertilization, this limitation is dependent  
697 only on the ambient CO<sub>2</sub> concentrations and could not represent the heterogeneous  
698 distribution of nutrients. As a result, the model could not reveal the biogeochemical  
699 effects of nitrogen and phosphorus deposition on land ecosystems. Second, the  
700 feedback of fire activities to ecosystems is ignored. The iMAPLE ~~model~~ considers the  
701 impacts of fuel load on area burned at each modeling time step. However, these fire  
702 perturbations do not in turn change the vegetation distribution and composition. The  
703 vegetation model does not consider the competition among PFTs, so that fire  
704 perturbations are not allowed to change vegetation coverage. As a result, the  
705 interactions between fire and ecosystems are underestimated in the current model  
706 framework, potentially leading to overestimations of wildfire activity due to  
707 remaining fuel loads.” Third, iMAPLE does not consider the dynamic changes in  
708 wetland area for CH<sub>4</sub> emissions. Although the Noah-MP module predicts runoff and  
709 underground water, the changes of hydrological cycles are not connected with wetland  
710 area in the model. Instead, a prescribed wetland dataset is applied to reduce the  
711 possible uncertainties but meanwhile limits the explorations of CH<sub>4</sub> changes in the  
712 historical and future periods. Meanwhile, ~~the~~ iMAPLE model considers only dynamic  
713 soil water and temperature ~~at-down to the~~ 2-m level, which may ~~influence-affect~~ the  
714 ~~deeper-soil~~ interactions between climate and ~~the~~ land terrestrial ecosystem especially  
715 ~~for-during~~ the drier conditions. These limitations will be the focuses of model

716 development in the next step.

717

718 The iMAPLE model inherits the good capability of the original YIBs model in the  
719 simulations of carbon cycle. Furthermore, ~~the~~iMAPLE upgrades the YIBs model with  
720 carbon-water coupling and more biogeochemical processes. With the iMAPLE model,  
721 we could assess the changes of carbon and water fluxes, as well as their coupling, in  
722 response to environmental perturbations (e.g., climate change, air pollution, land  
723 cover change). Meanwhile, by coupling ~~the~~iMAPLE with climate and/or chemical  
724 models, we could further quantify the changes of meteorology and atmospheric  
725 components in response to the biogeochemical and biogeophysical processes. For  
726 example, Lei et al. (2022) revealed the strong vegetation feedback to global surface  
727 O<sub>3</sub> during the drought periods using the YIBs model coupled to a chemical transport  
728 model. Xie et al. (2019) found a significant increase in atmospheric CO<sub>2</sub>  
729 concentrations due to O<sub>3</sub>-induced vegetation damage using the YIBs model coupled  
730 with a regional climate-chemistry model. Gong et al. (2021) estimated a surface  
731 warming in polluted regions due to the ozone-vegetation feedback using the YIBs  
732 model coupled with a global climate-chemistry model. These studies indicate that the  
733 iMAPLE model could be used either offline or online with other models to explore  
734 the interactions among climate, chemistry, and ecosystems.

735

736 *Acknowledgment.* This work was jointly supported by the National Key Research and  
737 Development Program of China (grant no. 2019YFA0606802), the National Natural  
738 Science Foundation of China (grant no. 42275128), and the Natural Science  
739 Foundation of Jiangsu Province (grant no. BK20220031).

740

741 *Author contributions.* XY designed the research and wrote the paper. XY, HaZ  
742 optimized codes, performed simulations, and analyzed results. HaZ, CT, YM, YH, CG  
743 implemented codes and collected data. HuZ helped with code implementations. All  
744 authors commented on and revised the manuscript.

745

746 *Competing interests.* The contact author has declared that none of the authors has any  
747 competing interests.

748

749 *Code availability.* The code for the iMAPLE version 1 model is available at  
750 <https://doi.org/10.6084/m9.figshare.23593578.v1>

751

752 *Data availability.* All the validation data are available to download from the cited  
753 references or data links shown in Section 2.4. The simulation data of monthly output  
754 from [the](#) BASE experiment during 1980-2021 with the iMAPLE model are available  
755 at <https://doi.org/10.6084/m9.figshare.23593578.v1>

756

## 757 **Reference**

758 Arora, V. K., Boer, G. J., Christian, J. R., Curry, C. L., Denman, K. L., Zahariev, K.,  
759 Flato, G. M., Scinocca, J. F., Merryfield, W. J., and Lee, W. G.: The Effect of  
760 Terrestrial Photosynthesis Down Regulation on the Twentieth-Century Carbon  
761 Budget Simulated with the CCCma Earth System Model, *J Climate*, 22, 6066-  
762 6088, 10.1175/2009jcli3037.1, 2009.

763 Ball, J. T., Woodrow, I. E., and Berry, J. A.: A model predicting stomatal conductance  
764 and its contribution to the control of photosynthesis under different  
765 environmental conditions, in: *Progress in Photosynthesis Research*, edited by:  
766 Biggins, J., Nijhoff, Dordrecht, Netherlands, 221-224, 1987.

767 Beer, C., Reichstein, M., Tomelleri, E., Ciais, P., Jung, M., Carvalhais, N., Rodenbeck,  
768 C., Arain, M. A., Baldocchi, D., Bonan, G. B., Bondeau, A., Cescatti, A., Lasslop,  
769 G., Lindroth, A., Lomas, M., Luysaert, S., Margolis, H., Oleson, K. W.,  
770 Rouspard, O., Veenendaal, E., Viovy, N., Williams, C., Woodward, F. I., and  
771 Papale, D.: Terrestrial Gross Carbon Dioxide Uptake: Global Distribution and  
772 Covariation with Climate, *Science*, 329, 834-838, 10.1126/Science.1184984,  
773 2010.

774 Cao, Y., Yue, X., Lei, Y., Zhou, H., Liao, H., Song, Y., Bai, J., Yang, Y., Chen, L., Zhu,  
775 J., Ma, Y., and Tian, C.: Identifying the drivers of modeling uncertainties in  
776 isoprene emissions: schemes versus meteorological forcings, *Journal of*  
777 *Geophysical Research*, 126, e2020JD034242, 10.1029/2020JD034242, 2021a.

778 Cao, Y., Yue, X., Liao, H., Yang, Y., Zhu, J., Chen, L., Tian, C., Lei, Y., Zhou, H., and  
779 Ma, Y.: Ensemble projection of global isoprene emissions by the end of 21<sup>st</sup>  
780 century using CMIP6 models, *Atmospheric Environment*, 267, 118766,  
781 10.1016/j.atmosenv.2021.118766, 2021b.

Formatted: Superscript



782 Carslaw, K. S., Boucher, O., Spracklen, D. V., Mann, G. W., Rae, J. G. L., Woodward,  
783 S., and Kulmala, M.: A review of natural aerosol interactions and feedbacks  
784 within the Earth system, *Atmos Chem Phys*, 10, 1701-1737, 10.5194/acp-10-  
785 1701-2010, 2010.

786 Castillo, C. K. G., Levis, S., and Thornton, P.: Evaluation of the New CNDV Option  
787 of the Community Land Model: Effects of Dynamic Vegetation and Interactive  
788 Nitrogen on CLM4 Means and Variability, *J Climate*, 25, 3702-3714,  
789 10.1175/Jcli-D-11-00372.1, 2012.

790 Chen, G., Guo, Y., Yue, X., Tong, S., Gasparrini, A., Bell, M. L., Armstrong, B.,  
791 Schwartz, J., Jouni J K Jaakkola, Zanobetti, A., Lavigne, E., Saldiva, P. H. N.,  
792 Kan, H., Royé, D., Milojevic, A., Overcenco, A., Urban, A., Schneider, A.,  
793 Entezari, A., Vicedo-Cabrera, A. M., Zeka, A., Tobias, A., Nunes, B., Alahmad, B.,  
794 Bertil Forsberg, Pan, S.-C., Íñiguez, C., Ameling, C., Valencia, C. D. I. C.,  
795 Åström, C., Houthuijs, D., Dung, D. V., Samoli, E., Mayvaneh, F., Sera, F.,  
796 Carrasco-Escobar, G., Lei, Y., Orru, H., Kim, H., Iulian-Horia Holobaca, Kysely,  
797 J., Teixeira, J. P., Madureira, J., Katsouyanni, K., Hurtado-Díaz, M., Maasikmets,  
798 M., Ragetti, M. S., Hashizume, M., Stafoggia, M., Pascal, M., Scortichini, M.,  
799 Micheline de Sousa Zanotti Stagliorio Coêlho, Ortega, N. V., Ryti, N. R. I.,  
800 Scovronick, N., Matus, P., Goodman, P., Garland, R. M., Abrutzky, R., Garcia, S.  
801 O., Rao, S., Fratianni, S., Dang, T. N., Colistro, V., Huber, V., Lee, W., Seposo, X.,  
802 Honda, Y., Guo, Y. L., Ye, T., Yu, W., Abramson, M. J., Samet, J. M., and Li, S.:  
803 Mortality risk attributable to wildfire-related PM<sub>2.5</sub> pollution: a global time  
804 series study in 749 locations, *The Lancet Planetary Health*, 5, e579-e587,  
805 10.1016/S2542-5196(21)00200-X, 2021.

806 Clapp, R. B., and Hornberger, G. M.: Empirical equations for some soil hydraulic  
807 properties, *Water Resources Research*, 14, 601-604, 1978.

808 Cox, P. M.: Description of the "TRIFFID" Dynamic Global Vegetation Model, Hadley  
809 Centre technical note 24, Berks, UK, 2001.

810 Defries, R. S., Hansen, M. C., Townshend, J. R. G., Janetos, A. C., and Loveland, T.  
811 R.: A new global 1-km dataset of percentage tree cover derived from remote  
812 sensing, *Global Change Biology*, 6, 247-254, 10.1046/j.1365-2486.2000.00296.x,  
813 2000.

814 Delwiche, K. B., Knox, S. H., Malhotra, A., Fluet-Chouinard, E., McNicol, G., Feron,  
815 S., Ouyang, Z., Papale, D., Trotta, C., Canfora, E., Cheah, Y. W., Christianson, D.,  
816 Alberto, M. C. R., Alekseychik, P., Aurela, M., Baldocchi, D., Bansal, S.,  
817 Billesbach, D. P., Bohrer, G., Bracho, R., Buchmann, N., Campbell, D. I., Celis,  
818 G., Chen, J., Chen, W., Chu, H., Dalmagro, H. J., Dengel, S., Desai, A. R., Detto,  
819 M., Dolman, H., Eichelmann, E., Euskirchen, E., Famulari, D., Fuchs, K.,  
820 Goeckede, M., Gogo, S., Gondwe, M. J., Goodrich, J. P., Gottschalk, P., Graham,  
821 S. L., Heimann, M., Helbig, M., Helfter, C., Hemes, K. S., Hirano, T., Hollinger,  
822 D., Hörtnagl, L., Iwata, H., Jacotot, A., Jurasinski, G., Kang, M., Kasak, K., King,  
823 J., Klatt, J., Koebisch, F., Krauss, K. W., Lai, D. Y. F., Lohila, A., Mammarella, I.,  
824 Beletti Marchesini, L., Manca, G., Matthes, J. H., Maximov, T., Merbold, L.,  
825 Mitra, B., Morin, T. H., Nemitz, E., Nilsson, M. B., Niu, S., Oechel, W. C.,

826 Oikawa, P. Y., Ono, K., Peichl, M., Peltola, O., Reba, M. L., Richardson, A. D.,  
827 Riley, W., Runkle, B. R. K., Ryu, Y., Sachs, T., Sakabe, A., Sanchez, C. R.,  
828 Schuur, E. A., Schäfer, K. V. R., Sonnentag, O., Sparks, J. P., Stuart-Haëntjens, E.,  
829 Sturtevant, C., Sullivan, R. C., Szutu, D. J., Thom, J. E., Torn, M. S., Tuittila, E.  
830 S., Turner, J., Ueyama, M., Valach, A. C., Vargas, R., Varlagin, A., Vazquez-Lule,  
831 A., Verfaillie, J. G., Vesala, T., Vourlitis, G. L., Ward, E. J., Wille, C., Wohlfahrt,  
832 G., Wong, G. X., Zhang, Z., Zona, D., Windham-Myers, L., Poulter, B., and  
833 Jackson, R. B.: FLUXNET-CH4: a global, multi-ecosystem dataset and analysis  
834 of methane seasonality from freshwater wetlands, *Earth Syst. Sci. Data*, 13, 3607-  
835 3689, 10.5194/essd-13-3607-2021, 2021.

836 Farquhar, G. D., Caemmerer, S. V., and Berry, J. A.: A biochemical-model of  
837 photosynthetic CO<sub>2</sub> assimilation in leaves of C-3 species, *Planta*, 149, 78-90,  
838 10.1007/bf00386231, 1980.

839 Friedlingstein, P., O'Sullivan, M., Jones, M. W., Andrew, R. M., Hauck, J., Olsen, A.,  
840 Peters, G. P., Peters, W., Pongratz, J., Sitch, S., Quéré, C. L., Canadell, J. G.,  
841 Ciais, P. P., Jackson, R. B., Alin, S., Aragao, L. E., Arneeth, A., Arora, V., Bates, N.  
842 R., Becker, M., Benoit-Cattin, A., Bittig, H. C., Bopp, L., Bultan, S., Chandra, N.,  
843 Chevallier, F., Chini, L. P., Evans, W., Florentie, L., Forster, P. M., Gasser, T.,  
844 Gehlen, M., Gilfillan, D., Gkritzalis, T., Gregor, L., Gruber, N., Harris, I.,  
845 Hartung, K., Haverd, V., Houghton, R. A., Ilyina, T., Jain, A. K., Joetzjer, E.,  
846 Kadono, K., Kato, E., Kitidis, V., Ivar, J. I. J., Landschützer, P., Lefèvre, N.,  
847 Lenton, A., Lienert, S., Liu, Z., Lombardozzi, D., Marland, G., Metzl, N., Munro,  
848 D. R., Nabel, J. E., Nakaoka, S.-I., Niwa, Y., O'Brien, K., Ono, T., Palmer, P. I.,  
849 Pierrot, D., Poulter, B., Resplandy, L., Robertson, E., Rödenbeck, C., Schwinger,  
850 J., Séférian, R., Skjelvan, I., Smith, A. J., Sutton, A., Tanhua, T., Tans, P. P., Tian,  
851 H., Tilbrook, B., Werf, G. R. v. d., Vuichard, N., Walker, A., Wanninkhof, R.,  
852 Watson, A. J., Willis, D., Wiltshire, A. J., Yuan, W., Yue, X., and Zaehle, S.:  
853 Global Carbon Budget 2020, *Earth System Science Data*, 12, 3269-3340, 2020.

854 Friedlingstein, P., O'Sullivan, M., Jones, M. W., Andrew, R. M., Gregor, L., Hauck, J.,  
855 Quéré, C. L., Luijkx, I. T., Olsen, A., Peters, G. P., Peters, W., Pongratz, J.,  
856 Schwingshackl, C., Sitch, S., Canadell, J. G., Ciais, P., Jackson, R. B., Alin, S. R.,  
857 Alkama, R., Arneeth, A., Arora, V. K., Bates, N. R., Becker, M., Bellouin, N.,  
858 Bittig, H. C., Bopp, L., Chevallier, F., Chini, L. P., Cronin, M., Decharme, B.,  
859 Evans, W., Falk, S., Feely, R. A., Gasser, T., Gehlen, M., Gkritzalis, T., Gloege, L.,  
860 Grassi, G., Gruber, N., Gürses, Ö., Harris, I., Hefner, M., Houghton, R. A., Hurtt,  
861 G. C., Iida, Y., Ilyina, T., Jain, A. K., Jersild, A., Kadono, K., Kato, E., Kennedy,  
862 D., Goldewijk, K. K., Knauer, J., Korsbakken, J. I., Landschützer, P., Lefèvre, N.,  
863 Lindsay, K., Liu, Z., Liu, J., Marland, G., Mayot, N., McGrath, M. J., Metzl, N.,  
864 Monacci, N. M., Munro, D. R., Nakaoka, S.-I., Niwa, Y., O'Brien, K., Ono, T.,  
865 Palmer, P. I., Pan, N., Pierrot, D., Pocock, K., Poulter, B., Resplandy, L.,  
866 Robertson, E., Rödenbeck, C., Rodriguez, C., Rosan, T. M., Schwinger, J.,  
867 Séférian, R., Shutler, J. D., Skjelvan, I., Steinhoff, T., Sun, Q., Sutton, A. J.,  
868 Sweeney, C., Takao, S., Tanhua, T., Tans, P. P., Tian, X., Tian, H., Tilbrook, B.,  
869 Tsujino, H., Tubiello, F., Werf, G. v. d., Walker, A. P., Wanninkhof, R., Whitehead,

870 C., Wranne, A. W., Wright, R., Yuan, W., Yue, C., Yue, X., Zaehle, S., Zeng, J.,  
871 and Zheng, B.: Global Carbon Budget 2022, *Earth System Science Data*, 14,  
872 4811-4900, 10.5194/essd-14-4811-2022, 2022.

873 Gelaro, R., McCarty, W., Suarez, M. J., Todling, R., Molod, A., Takacs, L., Randles, C.  
874 A., Darmenov, A., Bosilovich, M. G., Reichle, R., Wargan, K., Coy, L., Cullather,  
875 R., Draper, C., Akella, S., Buchard, V., Conaty, A., da Silva, A. M., Gu, W., Kim,  
876 G. K., Koster, R., Lucchesi, R., Merkova, D., Nielsen, J. E., Partyka, G., Pawson,  
877 S., Putman, W., Rienecker, M., Schubert, S. D., Sienkiewicz, M., and Zhao, B.:  
878 The Modern-Era Retrospective Analysis for Research and Applications, Version 2  
879 (MERRA-2), *J Climate*, 30, 5419-5454, 10.1175/Jcli-D-16-0758.1, 2017.

880 Gong, C., Liao, H., Yue, X., Ma, Y., and Lei, Y.: Impacts of ozone-vegetation  
881 interactions on ozone pollution episodes in North China and the Yangtze River  
882 Delta, *Geophysical Research Letters*, 48, e2021GL093814,  
883 10.1029/2021GL093814, 2021.

884 Guenther, A. B., Jiang, X., Heald, C. L., Sakulyanontvittaya, T., Duhl, T., Emmons, L.  
885 K., and Wang, X.: The Model of Emissions of Gases and Aerosols from Nature  
886 version 2.1 (MEGAN2.1): an extended and updated framework for modeling  
887 biogenic emissions, *Geosci Model Dev*, 5, 1471-1492, 10.5194/Gmd-5-1471-  
888 2012, 2012.

889 Hansen, M. C., DeFries, R. S., Townshend, J. R. G., Carroll, M., Dimiceli, C., and  
890 Sohlberg, R. A.: Global Percent Tree Cover at a Spatial Resolution of 500 Meters:  
891 First Results of the MODIS Vegetation Continuous Fields Algorithm, *Earth  
892 Interact*, 7, 1-15, 10.1175/1087-3562(2003)007<0001:GPTCAA>2.0.CO;2, 2003.

893 Heimann, I., Griffiths, P. T., Warwick, N. J., Abraham, N. L., Archibald, A. T., and  
894 Pyle, J. A.: Methane Emissions in a Chemistry-Climate Model: Feedbacks and  
895 Climate Response, *J Adv Model Earth Sy*, 12, e2019MS002019,  
896 10.1029/2019MS002019, 2020.

897 Hengl, T., de Jesus, J. M., Heuvelink, G. B. M., Gonzalez, M. R., Kilibarda, M.,  
898 Blagotic, A., Shangquan, W., Wright, M. N., Geng, X. Y., Bauer-Marschallinger,  
899 B., Guevara, M. A., Vargas, R., MacMillan, R. A., Batjes, N. H., Leenaars, J. G.  
900 B., Ribeiro, E., Wheeler, I., Mantel, S., and Kempen, B.: SoilGrids250m: Global  
901 gridded soil information based on machine learning, *Plos One*, 12, ARTN  
902 e0169748  
903 10.1371/journal.pone.0169748, 2017.

904 Jasechko, S., Sharp, Z. D., Gibson, J. J., Birks, S. J., Yi, Y., and Fawcett, P. J.:  
905 Terrestrial water fluxes dominated by transpiration, *Nature*, 496, 347-350,  
906 10.1038/nature11983, 2013.

907 Jung, M., Reichstein, M., Margolis, H. A., Cescatti, A., Richardson, A. D., Arain, M.  
908 A., Arneth, A., Bernhofer, C., Bonal, D., Chen, J. Q., Gianelle, D., Gobron, N.,  
909 Kiely, G., Kutsch, W., Lasslop, G., Law, B. E., Lindroth, A., Merbold, L.,  
910 Montagnani, L., Moors, E. J., Papale, D., Sottocornola, M., Vaccari, F., and  
911 Williams, C.: Global patterns of land-atmosphere fluxes of carbon dioxide, latent  
912 heat, and sensible heat derived from eddy covariance, satellite, and  
913 meteorological observations, *Journal of Geophysical Research*, 116, G00j07,

914 10.1029/2010jg001566, 2011.

915 Jung, M., Schwalm, C., Migliavacca, M., Walther, S., Camps-Valls, G., Koirala, S.,  
916 Anthoni, P., Besnard, S., Bodesheim, P., Carvalhais, N., Chevallier, F., Gans, F.,  
917 Goll, D. S., Haverd, V., Köhler, P., Ichii, K., Jain, A. K., Liu, J., Lombardozi, D.,  
918 Nabel, J. E. M. S., Nelson, J. A., O'Sullivan, M., Pallandt, M., Papale, D., Peters,  
919 W., Pongratz, J., Rödenbeck, C., Sitch, S., Tramontana, G., Walker, A., Weber, U.,  
920 and Reichstein, M.: Scaling carbon fluxes from eddy covariance sites to globe:  
921 synthesis and evaluation of the FLUXCOM approach, *Biogeosciences*, 17, 1343-  
922 1365, 10.5194/bg-17-1343-2020, 2020a.

923 Jung, M., Schwalm, C., Migliavacca, M., Walther, S., Camps-Valls, G., Koirala, S.,  
924 Anthoni, P., Besnard, S., Bodesheim, P., Carvalhais, N., Chevallier, F., Gans, F.,  
925 Goll, D. S., Haverd, V., Köhler, P., Ichii, K., Jain, A. K., Liu, J. Z., Lombardozi,  
926 D., Nabel, J. E. M. S., Nelson, J. A., O'Sullivan, M., Pallandt, M., Papale, D.,  
927 Peters, W., Pongratz, J., Rodenbeck, C., Sitch, S., Tramontana, G., Walker, A.,  
928 Weber, U., and Reichstein, M.: Scaling carbon fluxes from eddy covariance sites  
929 to globe: synthesis and evaluation of the FLUXCOM approach, *Biogeosciences*,  
930 17, 1343-1365, 10.5194/bg-17-1343-2020, 2020b.

931 Kattge, J., Diaz, S., Lavorel, S., Prentice, C., Leadley, P., Bonisch, G., Garnier, E.,  
932 Westoby, M., Reich, P. B., Wright, I. J., Cornelissen, J. H. C., Violle, C., Harrison,  
933 S. P., van Bodegom, P. M., Reichstein, M., Enquist, B. J., Soudzilovskaia, N. A.,  
934 Ackerly, D. D., Anand, M., Atkin, O., Bahn, M., Baker, T. R., Baldocchi, D.,  
935 Bekker, R., Blanco, C. C., Blonder, B., Bond, W. J., Bradstock, R., Bunker, D. E.,  
936 Casanoves, F., Cavender-Bares, J., Chambers, J. Q., Chapin, F. S., Chave, J.,  
937 Coomes, D., Cornwell, W. K., Craine, J. M., Dobrin, B. H., Duarte, L., Durka, W.,  
938 Elser, J., Esser, G., Estiarte, M., Fagan, W. F., Fang, J., Fernandez-Mendez, F.,  
939 Fidelis, A., Finegan, B., Flores, O., Ford, H., Frank, D., Freschet, G. T., Fyllas, N.  
940 M., Gallagher, R. V., Green, W. A., Gutierrez, A. G., Hickler, T., Higgins, S. I.,  
941 Hodgson, J. G., Jalili, A., Jansen, S., Joly, C. A., Kerkhoff, A. J., Kirkup, D.,  
942 Kitajima, K., Kleyer, M., Klotz, S., Knops, J. M. H., Kramer, K., Kuhn, I.,  
943 Kurokawa, H., Laughlin, D., Lee, T. D., Leishman, M., Lens, F., Lenz, T., Lewis,  
944 S. L., Lloyd, J., Llusia, J., Louault, F., Ma, S., Mahecha, M. D., Manning, P.,  
945 Massad, T., Medlyn, B. E., Messier, J., Moles, A. T., Muller, S. C., Nadrowski, K.,  
946 Naeem, S., Niinemets, U., Nollert, S., Nuske, A., Ogaya, R., Oleksyn, J.,  
947 Onipchenko, V. G., Onoda, Y., Ordonez, J., Overbeck, G., Ozinga, W. A., Patino,  
948 S., Paula, S., Pausas, J. G., Penuelas, J., Phillips, O. L., Pillar, V., Poorter, H.,  
949 Poorter, L., Poschlod, P., Prinzing, A., Proulx, R., Rammig, A., Reinsch, S., Reu,  
950 B., Sack, L., Salgado-Negre, B., Sardans, J., Shiodera, S., Shipley, B., Siefert, A.,  
951 Sosinski, E., Soussana, J. F., Swaine, E., Swenson, N., Thompson, K., Thornton,  
952 P., Waldram, M., Weiher, E., White, M., White, S., Wright, S. J., Yguel, B.,  
953 Zaehle, S., Zanne, A. E., and Wirth, C.: TRY - a global database of plant traits,  
954 *Global Change Biology*, 17, 2905-2935, 10.1111/j.1365-2486.2011.02451.x, 2011.

955 Keeling, C. D., Bacastow, R. B., Bainbridge, A. E., Ekdahl, C. A., Guenther, P. R.,  
956 Waterman, L. S., and Chin, J. F. S.: Atmospheric carbon dioxide variations at  
957 Mauna Loa Observatory, Hawaii, *Tellus A.*, 28, 538-551, 10.1111/j.2153-

958 3490.1976.tb00701.x, 1976.

959 Lei, Y., Yue, X., Liao, H., Gong, C., and Zhang, L.: Implementation of Yale  
960 Interactive terrestrial Biosphere model v1.0 into GEOS-Chem v12.0.0: a tool for  
961 biosphere-chemistry interactions, *Geosci Model Dev*, 13, 1137-1153,  
962 10.5194/gmd-13-1137-2020, 2020.

963 Lei, Y., Yue, X., Liao, H., Zhang, L., Zhou, H., Tian, C., Gong, C., Ma, Y., Cao, Y.,  
964 Seco, R., Karl, T., and Potosnak, M.: Global perspective of drought impacts on  
965 ozone pollution episodes, *Environmental Science & Technology*, 56, 3932-3940,  
966 2022.

967 Li, F., Zeng, X. D., and Levis, S.: A process-based fire parameterization of  
968 intermediate complexity in a Dynamic Global Vegetation Model (vol 9, pg 2761,  
969 2012), *Biogeosciences*, 9, 4771-4772, 10.5194/bg-9-4771-2012, 2012.

970 Li, X., and Xiao, J.: Mapping Photosynthesis Solely from Solar-Induced Chlorophyll  
971 Fluorescence: A Global, Fine-Resolution Dataset of Gross Primary Production  
972 Derived from OCO-2, *Remote Sensing*, 11, 2563, 10.3390/rs11212563, 2019.

973 Lin, M. Y., Horowitz, L. W., Xie, Y. Y., Paulot, F., Malyshev, S., Shevliakova, E.,  
974 Finco, A., Gerosa, G., Kubistin, D., and Pilegaard, K.: Vegetation feedbacks  
975 during drought exacerbate ozone air pollution extremes in Europe, *Nat Clim*  
976 *Change*, 10, 444-451, 10.1038/s41558-020-0743-y, 2020.

977 Lombardozi, D., Levis, S., Bonan, G., Hess, P. G., and Sparks, J. P.: The Influence of  
978 Chronic Ozone Exposure on Global Carbon and Water Cycles, *J Climate*, 28,  
979 292-305, 10.1175/Jcli-D-14-00223.1, 2015.

980 Ma, Y., Yue, X., Zhou, H., Gong, C., Lei, Y., Tian, C., and Cao, Y.: Identifying the  
981 dominant climate-driven uncertainties in modeling gross primary productivity,  
982 *Science of the Total Environment*, 800, 149518, 10.1016/j.scitotenv.2021.149518,  
983 2021.

984 Ma, Y., Yue, X., Sitch, S., Unger, N., Uddling, J., Mercado, L. M., Gong, C., Feng, Z.,  
985 Yang, H., Zhou, H., Tian, C., Cao, Y., Lei, Y., Cheesman, A. W., Xu, Y., and Rojas,  
986 M. C. D.: Implementation of trait-based ozone plant sensitivity in the Yale  
987 Interactive terrestrial Biosphere model v1.0 to assess global vegetation damage,  
988 *Geosci Model Dev*, 16, 2261-2276, 10.5194/gmd-16-2261-2023, 2023.

989 Madani, N., Kimball, J. S., and Running, S. W.: Improving Global Gross Primary  
990 Productivity Estimates by Computing Optimum Light Use Efficiencies Using  
991 Flux Tower Data, *Journal of Geophysical Research-Biogeosciences*, 122, 2939-  
992 2951, 10.1002/2017jg004142, 2017.

993 Mercado, L. M., Bellouin, N., Sitch, S., Boucher, O., Huntingford, C., Wild, M., and  
994 Cox, P. M.: Impact of changes in diffuse radiation on the global land carbon sink,  
995 *Nature*, 458, 1014-U1087, 10.1038/Nature07949, 2009.

996 Moreno-Martínez, Á., Camps-Valls, G., Kattge, J., Robinson, N., Reichstein, M.,  
997 Bodegom, P. V., and Running, S. W.: Global maps of leaf traits at 3km resolution,  
998 TRY File Archive, in, 2018.

999 Niu, G. Y., Yang, Z. L., Mitchell, K. E., Chen, F., Ek, M. B., Barlage, M., Kumar, A.,  
1000 Manning, K., Niyogi, D., Rosero, E., Tewari, M., and Xia, Y. L.: The community  
1001 Noah land surface model with multiparameterization options (Noah-MP): 1.

1002 Model description and evaluation with local-scale measurements, *Journal of*  
1003 *Geophysical Research*, 116, D12109, 10.1029/2010jd015139, 2011.

1004 Paudel, R., Mahowald, N. M., Hess, P. G. M., Meng, L., and Riley, W. J.: Attribution  
1005 of changes in global wetland methane emissions from pre-industrial to present  
1006 using CLM4.5-BGC, *Environ Res Lett*, 11, 034020, 10.1088/1748-  
1007 9326/11/3/034020, 2016.

1008 Pechony, O., and Shindell, D. T.: Fire parameterization on a global scale, *Journal of*  
1009 *Geophysical Research-Atmospheres*, 114, D16115, 10.1029/2009jd011927, 2009.

1010 Piao, S. L., Ciais, P., Friedlingstein, P., de Noblet-Ducoudre, N., Cadule, P., Viovy, N.,  
1011 and Wang, T.: Spatiotemporal patterns of terrestrial carbon cycle during the 20th  
1012 century, *Global Biogeochem Cy*, 23, Gb4026, 10.1029/2008gb003339, 2009.

1013 Randerson, J. T., Chen, Y., van der Werf, G. R., Rogers, B. M., and Morton, D. C.:  
1014 Global burned area and biomass burning emissions from small fires, *Journal of*  
1015 *Geophysical Research-Biogeosciences*, 117, G04012, 10.1029/2012jg002128,  
1016 2012.

1017 Rap, A., Scott, C. E., Reddington, C. L., Mercado, L., Ellis, R. J., Garraway, S., Evans,  
1018 M. J., Beerling, D. J., MacKenzie, A. R., Hewitt, C. N., and Spracklen, D. V.:  
1019 Enhanced global primary production by biogenic aerosol via diffuse radiation  
1020 fertilization, *Nat Geosci*, 11, 640-644, 10.1038/s41561-018-0208-3, 2018.

1021 Rosentreter, J. A., Borges, A. V., Deemer, B. R., Holgerson, M. A., Liu, S. D., Song, C.  
1022 L., Melack, J., Raymond, P. A., Duarte, C. M., Allen, G. H., Olefeldt, D., Poulter,  
1023 B., Battin, T. I., and Eyre, B. D.: Half of global methane emissions come from  
1024 highly variable aquatic ecosystem sources, *Nature Geoscience*, 14, 225-+,  
1025 10.1038/s41561-021-00715-2, 2021.

1026 Running, S., Nemani, R., Heinsch, F., Zhao, M., Reeves, M., and Hashimoto, H.: A  
1027 continuous satellite-derived measure of global terrestrial primary production,  
1028 *BioScience*, 54, 547-560, 10.1641/0006-  
1029 3568(2004)054[0547:ACSMOG]2.0.CO;2, 2004.

1030 Saunois, M., Stavert, A. R., Poulter, B., Bousquet, P., Canadell, J. G., Jackson, R. B.,  
1031 Raymond, P. A., Dlugokencky, E. J., Houweling, S., Patra, P. K., Ciais, P., Arora,  
1032 V. K., Bastviken, D., Bergamaschi, P., Blake, D. R., Brailsford, G., Bruhwiler, L.,  
1033 Carlson, K. M., Carrol, M., Castaldi, S., Chandra, N., Crevoisier, C., Crill, P. M.,  
1034 Covey, K., Curry, C. L., Etiope, G., Frankenberg, C., Gedney, N., Hegglin, M. I.,  
1035 Hoglund-Isaksson, L., Hugelius, G., Ishizawa, M., Ito, A., Janssens-Maenhout, G.,  
1036 Jensen, K. M., Joos, F., Kleinen, T., Krummel, P. B., Langenfelds, R. L., Laruelle,  
1037 G. G., Liu, L. C., Machida, T., Maksyutov, S., McDonald, K. C., McNorton, J.,  
1038 Miller, P. A., Melton, J. R., Morino, I., Muller, J., Murguia-Flores, F., Naik, V.,  
1039 Niwa, Y., Noce, S., Doherty, S. O., Parker, R. J., Peng, C. H., Peng, S. S., Peters,  
1040 G. P., Prigent, C., Prinn, R., Ramonet, M., Regnier, P., Riley, W. J., Rosentreter, J.  
1041 A., Segers, A., Simpson, I. J., Shi, H., Smith, S. J., Steele, L. P., Thornton, B. F.,  
1042 Tian, H. Q., Tohjima, Y., Tubiello, F. N., Tsuruta, A., Viovy, N., Voulgarakis, A.,  
1043 Weber, T. S., van Weele, M., van der Werf, G. R., Weiss, R. F., Worthy, D.,  
1044 Wunch, D., Yin, Y., Yoshida, Y., Zhang, W. X., Zhang, Z., Zhao, Y. H., Zheng, B.,  
1045 Zhu, Q., Zhu, Q. A., and Zhuang, Q. L.: The Global Methane Budget 2000-2017,

1046 Earth System Science Data, 12, 1561-1623, 10.5194/essd-12-1561-2020, 2020.  
1047 Schaake, J. C., Koren, V. I., Duan, Q.-Y., Mitchell, K., and Chen, F.: Simple water  
1048 balance model for estimating runoff at different spatial and temporal scales,  
1049 Journal of Geophysical Research, 101, 7461-7475, 10.1029/95JD02892, 1996.  
1050 Schaefer, K., Collatz, G. J., Tans, P., Denning, A. S., Baker, I., Berry, J., Prihodko, L.,  
1051 Suits, N., and Philpott, A.: Combined Simple Biosphere/Carnegie-Ames-Stanford  
1052 Approach terrestrial carbon cycle model, J Geophys Res-Biogeo, 113, G03034,  
1053 10.1029/2007jg000603, 2008.  
1054 Scholes, R. J., Colstoun, E. B. d., Hall, F. G., Collatz, G. J., Meeson, B. W., Los, S. O.,  
1055 and Landis, D. R.: ISLSCP II Global Gridded Soil Characteristics, in, ORNL  
1056 DAAC, Oak Ridge, Tennessee, USA, 2011.  
1057 Sitch, S., Cox, P. M., Collins, W. J., and Huntingford, C.: Indirect radiative forcing of  
1058 climate change through ozone effects on the land-carbon sink, Nature, 448, 791-  
1059 U794, 10.1038/nature06059, 2007.  
1060 Sitch, S., Friedlingstein, P., Gruber, N., Jones, S. D., Murray-Tortarolo, G., Ahlström,  
1061 A., Doney, S. C., Graven, H., Heinze, C., Huntingford, C., Levis, S., Levy, P. E.,  
1062 Lomas, M., Poulter, B., Viovy, N., Zaehle, S., Zeng, N., Arneth, A., Bonan, G.,  
1063 Bopp, L., Canadell, J. G., Chevallier, F., Ciais, P., Ellis, R., Gloor, M., Peylin, P.,  
1064 Piao, S. L., Quéré, C. L., Smith, B., Zhu, Z., and Myneni, R.: Recent trends and  
1065 drivers of regional sources and sinks of carbon dioxide, Biogeosciences, 12, 653-  
1066 679, 2015.  
1067 Spitters, C. J. T.: Separating the Diffuse and Direct Component of Global Radiation  
1068 and Its Implications for Modeling Canopy Photosynthesis .2. Calculation of  
1069 Canopy Photosynthesis, Agr Forest Meteorol, 38, 231-242, 10.1016/0168-  
1070 1923(86)90061-4, 1986.  
1071 Spracklen, D. V., Arnold, S. R., and Taylor, C. M.: Observations of increased tropical  
1072 rainfall preceded by air passage over forests, Nature, 489, 282-U127, 2012.  
1073 Terrer, C., Jackson, R. B., Prentice, I. C., Keenan, T. F., Kaiser, C., Vicca, S., Fisher, J.  
1074 B., Reich, P. B., Stocker, B. D., Hungate, B. A., Penuelas, J., McCallum, I.,  
1075 Soudzilovskaia, N. A., Cernusak, L. A., Talhelm, A. F., Van Sundert, K., Piao, S.  
1076 L., Newton, P. C. D., Hovenden, M. J., Blumenthal, D. M., Liu, Y. Y., Muller, C.,  
1077 Winter, K., Field, C. B., Viechtbauer, W., Van Lissa, C. J., Hoosbeek, M. R.,  
1078 Watanabe, M., Koike, T., Leshyk, V. O., Polley, H. W., and Franklin, O.: Nitrogen  
1079 and phosphorus constrain the CO<sub>2</sub> fertilization of global plant biomass, Nat Clim  
1080 Change, 9, 684-689, 10.1038/s41558-019-0545-2, 2019.  
1081 Tian, C., Yue, X., Zhu, J., Liao, H., Yang, Y., Lei, Y., Zhou, X., Zhou, H., Ma, Y., and  
1082 Cao, Y.: Fire-climate interactions through aerosol radiative effect in a global  
1083 chemistry-climate-vegetation model, Atmospheric Chemistry and Physics, 22,  
1084 12353-12366, 10.5194/acp-22-12353-2022, 2022.  
1085 Tian, C., Yue, X., Zhu, J., Liao, H., Yang, Y., Chen, L., Zhou, X., Lei, Y., Zhou, H.,  
1086 and Cao, Y.: Projections of fire emissions and the consequent impacts on air  
1087 quality under 1.5°C and 2°C global warming, Environ Pollut, 323, 121311,  
1088 10.1016/j.envpol.2023.121311, 2023.  
1089 Unger, N., Harper, K., Zheng, Y., Kiang, N. Y., Aleinov, I., Arneth, A., Schurgers, G.,

1090 Amelynck, C., Goldstein, A., Guenther, A., Heinesch, B., Hewitt, C. N., Karl, T.,  
 1091 Laffineur, Q., Langford, B., McKinney, K. A., Misztal, P., Potosnak, M., Rinne, J.,  
 1092 Pressley, S., Schoon, N., and Serça, D.: Photosynthesis-dependent isoprene  
 1093 emission from leaf to planet in a global carbon–chemistry–climate model, *Atmos.*  
 1094 *Chem. Phys.*, 13, 10243-10269, 10.5194/acp-13-10243-2013, 2013.  
 1095 van der Werf, G. R., Randerson, J. T., Giglio, L., Collatz, G. J., Mu, M., Kasibhatla, P.  
 1096 S., Morton, D. C., DeFries, R. S., Jin, Y., and van Leeuwen, T. T.: Global fire  
 1097 emissions and the contribution of deforestation, savanna, forest, agricultural, and  
 1098 peat fires (1997-2009), *Atmos Chem Phys*, 10, 11707-11735, 10.5194/Acp-10-  
 1099 11707-2010, 2010.  
 1100 Walter, B. P., and Heimann, M.: A process-based, climate-sensitive model to derive  
 1101 methane emissions from natural wetlands: Application to five wetland sites,  
 1102 sensitivity to model parameters, and climate, *Global Biogeochem Cy*, 14, 745-  
 1103 765, 10.1029/1999GB001204, 2000.  
 1104 Walter, B. P., Heimann, M., and Matthews, E.: Modeling modern methane emissions  
 1105 from natural wetlands: 1. Model description and results, *Journal of Geophysical*  
 1106 *Research*, 106, 34189-34206, 10.1029/2001JD900165, 2001.  
 1107 Wang, B., Yue, X., Zhou, H., Lu, X., and Zhu, J.: Enhanced ecosystem water-use  
 1108 efficiency under the more diffuse radiation conditions, *Global Biogeochemical*  
 1109 *Cycles*, 37, e2022GB007606, 10.1029/2022GB007606, 2023.  
 1110 Wang, S. H., Zhang, Y. G., Ju, W. M., Chen, J. M., Ciais, P., Cescatti, A., Sardans, J.,  
 1111 Janssens, I. A., Wu, M. S., Berry, J. A., Campbell, E., Fernandez-Martinez, M.,  
 1112 Alkama, R., Sftch, S., Friedlingstein, P., Smith, W. K., Yuan, W. P., He, W.,  
 1113 Lombardozzi, D., Kautz, M., Zhu, D., Lienert, S., Kato, E., Poulter, B., Sanders,  
 1114 T. G. M., Kruger, I., Wang, R., Zeng, N., Tian, H. Q., Vuichard, N., Jain, A. K.,  
 1115 Wiltshire, A., Haverd, V., Goll, D. S., and Penuelas, J.: Recent global decline of  
 1116 CO<sub>2</sub> fertilization effects on vegetation photosynthesis, *Science*, 370, 1295-1300,  
 1117 10.1126/science.abb7772, 2020.  
 1118 Wania, R., Ross, I., and Prentice, I. C.: Implementation and evaluation of a new  
 1119 methane model within a dynamic global vegetation model: LPJ-WHyMe v1.3.1,  
 1120 *Geosci Model Dev*, 3, 565-584, 10.5194/gmd-3-565-2010, 2010.  
 1121 Warneke, C., Schwarz, J. P., Dibb, J., Kalashnikova, O., Frost, G., Al-Saad, J., Brown,  
 1122 S. S., Brewer, W. A., Soja, A., Seidel, F. C., Washenfelder, R. A., Wiggins, E. B.,  
 1123 Moore, R. H., Anderson, B. E., Jordan, C., Yacovitch, T. I., Herndon, S. C., Liu,  
 1124 S., Kuwayama, T., Jaffe, D., Johnston, N., Selimovic, V., Yokelson, R., Giles, D.  
 1125 M., Holben, B. N., Goloub, P., Popovici, I., Trainer, M., Kumar, A., Pierce, R. B.,  
 1126 Fahey, D., Roberts, J., Gargulinski, E. M., Peterson, D. A., Ye, X. X., Thapa, L.  
 1127 H., Saide, P. E., Fite, C. H., Holmes, C. D., Wang, S. Y., Coggon, M. M., Decker,  
 1128 Z. C. J., Stockwell, C. E., Xu, L., Gkatzelis, G., Aikin, K., Lefer, B., Kaspari, J.,  
 1129 Griffin, D., Zeng, L. H., Weber, R., Hastings, M., Chai, J. J., Wolfe, G. M.,  
 1130 Hanisco, T. F., Liao, J., Jost, P. C., Guo, H. Y., Jimenez, J. L., Crawford, J., and  
 1131 Team, F.-A. S.: Fire Influence on Regional to Global Environments and Air  
 1132 Quality (FIREX-AQ), *Journal of Geophysical Research*, 128, e2022JD037758,  
 1133 10.1029/2022JD037758, 2023.



1134 Worden, J., Saatchi, S., Keller, M., Bloom, A. A., Liu, J., Parazoo, N., Fisher, J. B.,  
1135 Bowman, K., Reager, J. T., Fahy, K., Schimel, D., Fu, R., Worden, S., Yin, Y.,  
1136 Gentine, P., Konings, A. G., Quetin, G. R., Williams, M., Worden, H., Shi, M. J.,  
1137 and Barkhordarian, A.: Satellite Observations of the Tropical Terrestrial Carbon  
1138 Balance and Interactions With the Water Cycle During the 21st Century, *Rev*  
1139 *Geophys*, 59, e2020RG000711, 10.1029/2020RG000711, 2021.

1140 Wu, K., Yang, X. Y., Chen, D., Gu, S., Lu, Y. Q., Jiang, Q., Wang, K., Ou, Y. H., Qian,  
1141 Y., Shao, P., and Lu, S. H.: Estimation of biogenic VOC emissions and their  
1142 corresponding impact on ozone and secondary organic aerosol formation in China,  
1143 *Atmos Res*, 231, 104656, 10.1016/j.atmosres.2019.104656, 2020.

1144 Xie, X., Wang, T., Yue, X., Li, S., Zhuang, B., Wang, M., and Yang, X.: Numerical  
1145 modeling of ozone damage to plants and its effects on atmospheric CO<sub>2</sub> in China,  
1146 *Atmospheric Environment*, 217, 116970, 10.1016/j.atmosenv.2019.116970, 2019.

1147 Yuan, W. P., Liu, S. G., Yu, G. R., Bonnefond, J. M., Chen, J. Q., Davis, K., Desai, A.  
1148 R., Goldstein, A. H., Gianelle, D., Rossi, F., Suyker, A. E., and Verma, S. B.:  
1149 Global estimates of evapotranspiration and gross primary production based on  
1150 MODIS and global meteorology data, *Remote Sensing of Environment*, 114,  
1151 1416-1431, 2010.

1152 Yuan, X. Y., Calatayud, V., Gao, F., Fares, S., Paoletti, E., Tian, Y., and Feng, Z. Z.:  
1153 Interaction of drought and ozone exposure on isoprene emission from extensively  
1154 cultivated poplar, *Plant Cell Environ*, 39, 2276-2287, 10.1111/pce.12798, 2016.

1155 Yue, X., and Unger, N.: Ozone vegetation damage effects on gross primary  
1156 productivity in the United States, *Atmospheric Chemistry and Physics*, 14, 9137-  
1157 9153, 10.5194/acp-14-9137-2014, 2014.

1158 Yue, X., and Unger, N.: The Yale Interactive terrestrial Biosphere model version 1.0:  
1159 description, evaluation and implementation into NASA GISS ModelE2, *Geosci*  
1160 *Model Dev*, 8, 2399-2417, 10.5194/gmd-8-2399-2015, 2015.

1161 Yue, X., Unger, N., Keenan, T. F., Zhang, X., and Vogel, C. S.: Probing the past 30-  
1162 year phenology trend of U.S. deciduous forests, *Biogeosciences*, 12, 4693-4709,  
1163 10.5194/bg-12-4693-2015, 2015.

1164 Yue, X., Keenan, T. F., Munger, W., and Unger, N.: Limited effect of ozone reductions  
1165 on the 20-year photosynthesis trend at Harvard forest, *Global Change Biology*, 22,  
1166 3750-3759, 10.1111/gcb.13300, 2016.

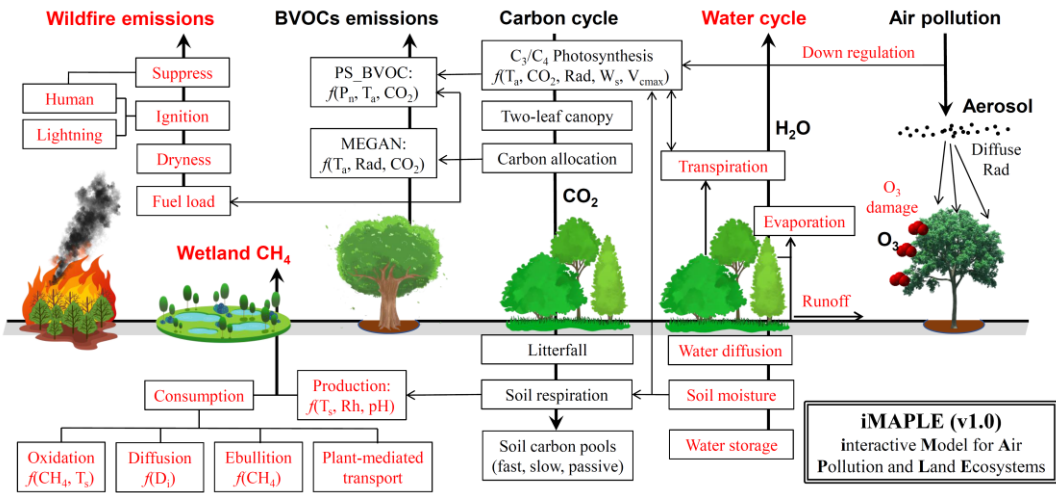
1167 Yue, X., and Unger, N.: Aerosol optical depth thresholds as a tool to assess diffuse  
1168 radiation fertilization of the land carbon uptake in China, *Atmospheric Chemistry*  
1169 *and Physics*, 17, 1329-1342, 10.5194/acp-17-1329-2017, 2017.

1170 Yue, X., Unger, N., Harper, K., Xia, X., Liao, H., Zhu, T., Xiao, J., Feng, Z., and Li, J.:  
1171 Ozone and haze pollution weakens net primary productivity in China,  
1172 *Atmospheric Chemistry and Physics*, 17, 6073-6089, 10.5194/acp-17-6073-2017,  
1173 2017.

1174 Yue, X., and Unger, N.: Fire air pollution reduces global terrestrial productivity,  
1175 *Nature Communications*, 9, 5413, 10.1038/s41467-018-07921-4, 2018.

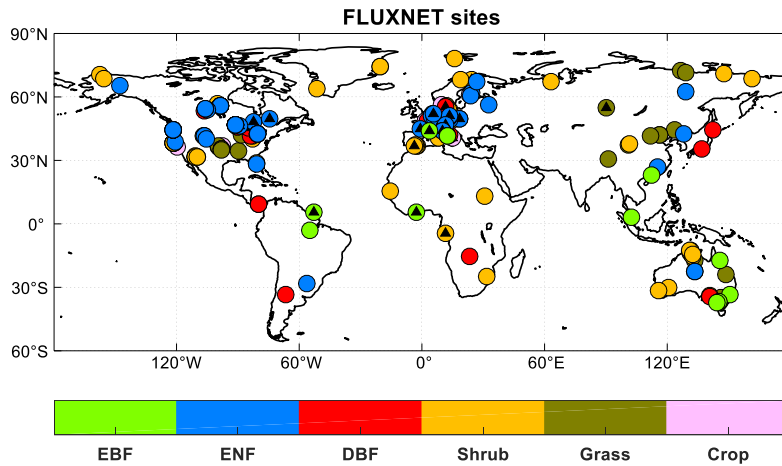
1176 Yue, X., Zhang, T., and Shao, C.: Afforestation increases ecosystem productivity and  
1177 carbon storage in China during the 2000s, *Agricultural and Forest Meteorology*,

1178 296, 108227, 10.1016/j.agrformet.2020.108227, 2021.  
1179 Zhang, Y., Li, C., Trettin, C. C., Li, H., and Sun, G.: An integrated model of soil,  
1180 hydrology, and vegetation for carbon dynamics in wetland ecosystems, *Global*  
1181 *Biogeochemical Cycles*, 16, 9-1-9-17, <https://doi.org/10.1029/2001GB001838>,  
1182 2002.  
1183 Zhang, Z., Zimmermann, N. E., Stenke, A., Li, X., Hodson, E. L., Zhu, G. F., Huang,  
1184 C. L., and Poulter, B.: Emerging role of wetland methane emissions in driving  
1185 21st century climate change, *P Natl Acad Sci USA*, 114, 9647-9652,  
1186 10.1073/pnas.1618765114, 2017.  
1187 Zhang, Z., Fluet-Chouinard, E., Jensen, K., McDonald, K., Hugelius, G., Gumbrecht,  
1188 T., Carroll, M., Prigent, C., Bartsch, A., and Poulter, B.: Development of the  
1189 global dataset of Wetland Area and Dynamics for Methane Modeling (WAD2M),  
1190 *Earth System Science Data*, 13, 2001-2023, 10.5194/essd-13-2001-2021, 2021.  
1191 Zhu, Q., Liu, J., Peng, C., Chen, H., Fang, X., Jiang, H., Yang, G., Zhu, D., Wang, W.,  
1192 and Zhou, X.: Modelling methane emissions from natural wetlands by  
1193 development and application of the TRIPLEX-GHG model, *Geosci Model Dev*, 7,  
1194 981-999, 10.5194/gmd-7-981-2014, 2014.  
1195 Zhuang, Q., Melillo, J. M., Kicklighter, D. W., Prinn, R. G., McGuire, A. D., Steudler,  
1196 P. A., Felzer, B. S., and Hu, S.: Methane fluxes between terrestrial ecosystems  
1197 and the atmosphere at northern high latitudes during the past century: A  
1198 retrospective analysis with a process-based biogeochemistry model, *Global*  
1199 *Biogeochem Cy*, 18, GB3010, 10.1029/2004GB002239, 2004.  
1200  
1201

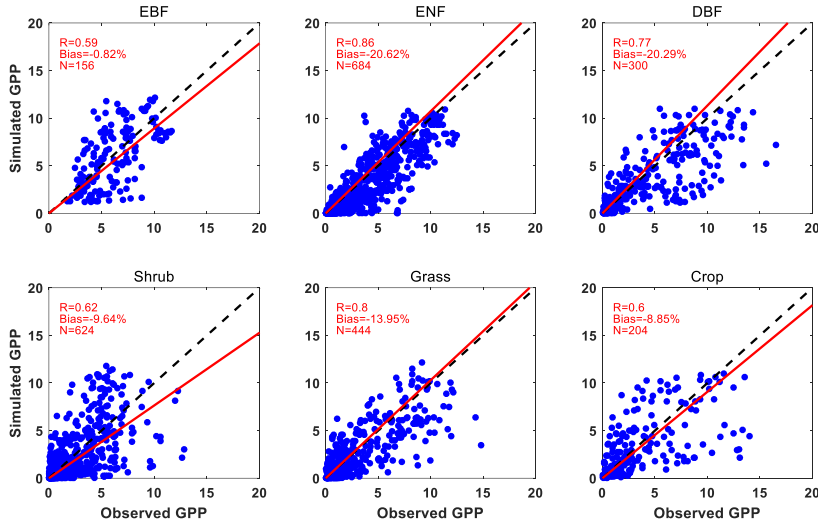


1204 **Figure 1** The illustration of biogeochemical processes in the iMAPLE version 1.0  
 1205 model. The carbon cycle is connected with water cycle, wildfire emissions, biogenic  
 1206 volatile organic compounds (BVOCs) emissions, wetland methane emissions, and is  
 1207 affected by air pollutants including aerosols and ozone. The bold arrows indicate the  
 1208 directions of fluxes and air pollutants. The thin arrows indicate the influential  
 1209 pathways among different components. The dependences on key parameters are  
 1210 shown for some processes. Red fonts indicate new or updated processes in iMAPLE  
 1211 relative to the YIBs model. For detailed parameterizations please refer to section 2.2.

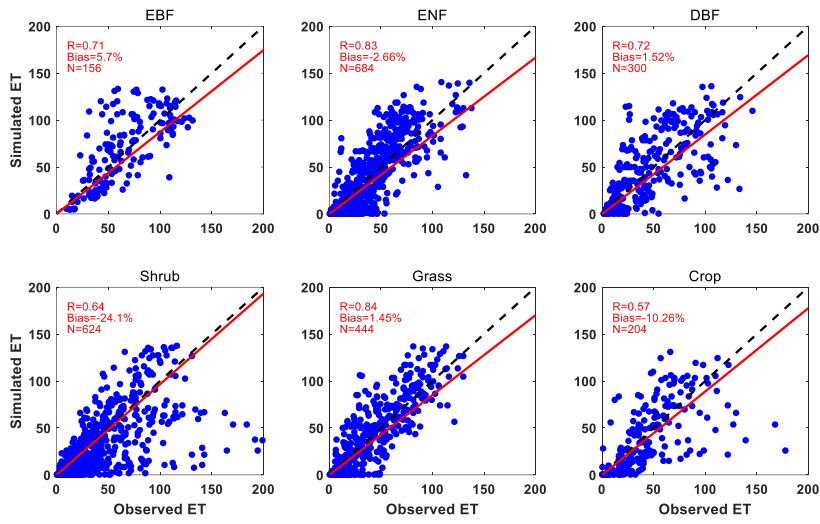
1212  
 1213  
 1214



1215  
 1216 **Figure 2** Spatial distributions of 201 sites from global FLUXNET network. The colors indicate  
 1217 various plant functional types (PFTs) including evergreen broadleaf forest (EBF, 13 sites),  
 1218 evergreen needleleaf forest (ENF, 57 sites), deciduous broadleaf forest (DBF, 25 sites), Shrub (52  
 1219 sites), Grass (37 sites), and Crop (17 sites). The black triangles indicate sites with at least one-year  
 1220 observations of diffuse radiation.  
 1221  
 1222

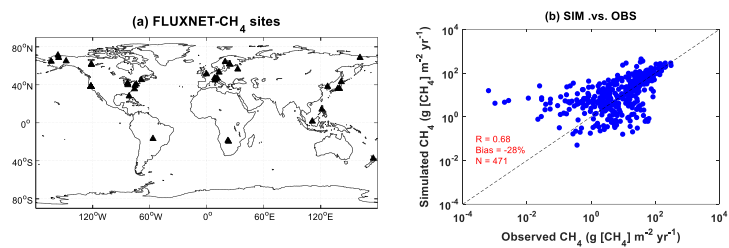


1223  
 1224 **Figure 3** Comparisons between observed and simulated monthly GPP from 201 FLUXNET sites.  
 1225 Each point indicates the average value of one month at a site. The red line represents linear  
 1226 regression between observations and simulations from the BASE experiment. The correlation  
 1227 coefficient (R), normalized mean bias and numbers of points/months (N) are shown on each panel.  
 1228 The comparisons are grouped into six PFTs including EBF, ENF, DBF, Shrub, Grass, and Crop.  
 1229 The unit is  $\text{g C m}^{-2} \text{ day}^{-1}$ .  
 1230



1231  
 1232  
 1233  
 1234

**Figure 4** The same as Figure 3 but for ET. The unit is mm month<sup>-1</sup>.



1235

1236

1237

1238

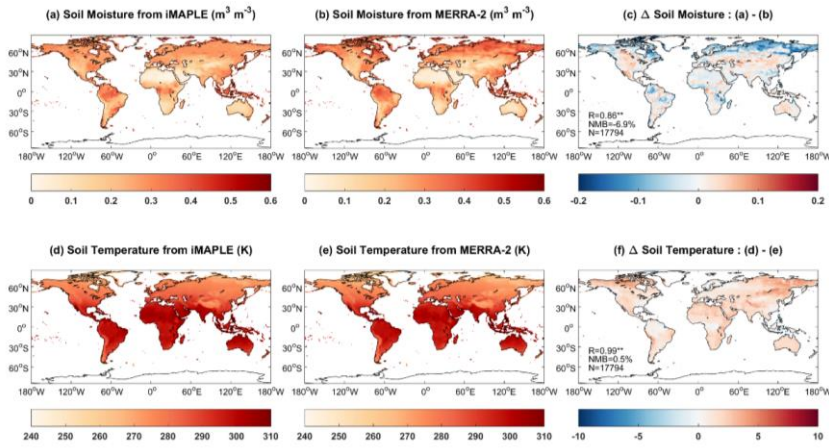
1239

1240

1241

1242

**Figure 5** (a) Spatial distribution of global FLUXNET-CH<sub>4</sub> sites and (b) comparisons between observed and simulated monthly methane flux from the BASE experiment. Filled triangles indicate sites with at least six months observations of wetland CH<sub>4</sub> fluxes. Each point represents average value of monthly methane emission at one site. The correlation coefficient (R), normalized mean bias and numbers of points/months (N) are shown on the right panel. The unit is g [CH<sub>4</sub>] m<sup>-2</sup> yr<sup>-1</sup>.



1243

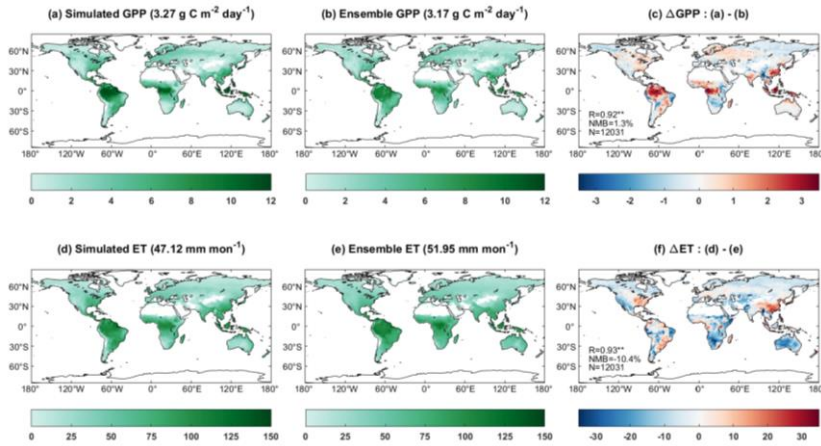
1244 **Figure 6** Comparisons of simulated (a) soil moisture ( $\text{m}^3 \text{m}^{-3}$ ) and (d) soil temperature (K) from  
 1245 the iMAPLE model with (b, e) the MERRA-2 reanalyses. Both simulations from the BASE  
 1246 experiment and observations from MERRA-2 reanalyses are averaged for the period of 1980-2020.  
 1247 The spatial difference, correlation coefficient (R), normalized mean bias (NMB) between  
 1248 simulations and observations and numbers of points (N) are shown on (c) and (f), respectively.

1249

1250

1251





1252

1253

1254

1255

1256

1257

1258

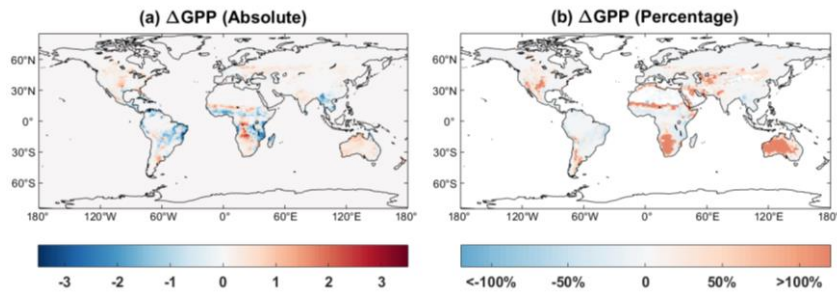
1259

1260

1261

1262

**Figure 7** Comparisons of simulated (a) gross primary productivity (GPP,  $\text{g C m}^{-2} \text{ day}^{-1}$ ) and (d) evapotranspiration (ET,  $\text{mm month}^{-1}$ ) with ensemble products from (b, e) observations. Simulated GPP and ET are performed by iMAPLE driven with meteorology from MERRA-2 reanalysis (BASE) during 2001-2013. Ensemble GPP products are from the average values of SIF-based GOSIF and satellite-based GLASS GPP products. Ensemble ET products include FLUXCOM and GLASS products during 2001-2013. The spatial difference, correlation coefficient (R), normalized mean bias (NMB) between simulations and observations and numbers of points (N) are shown on (c) and (f). Only land grids with vegetation are shown on each panel, and their area-weighted values are shown in titles.



1263

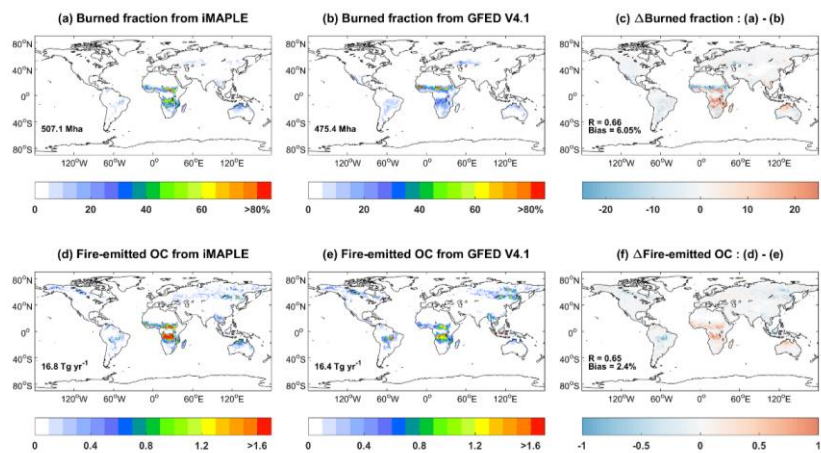
1264

1265

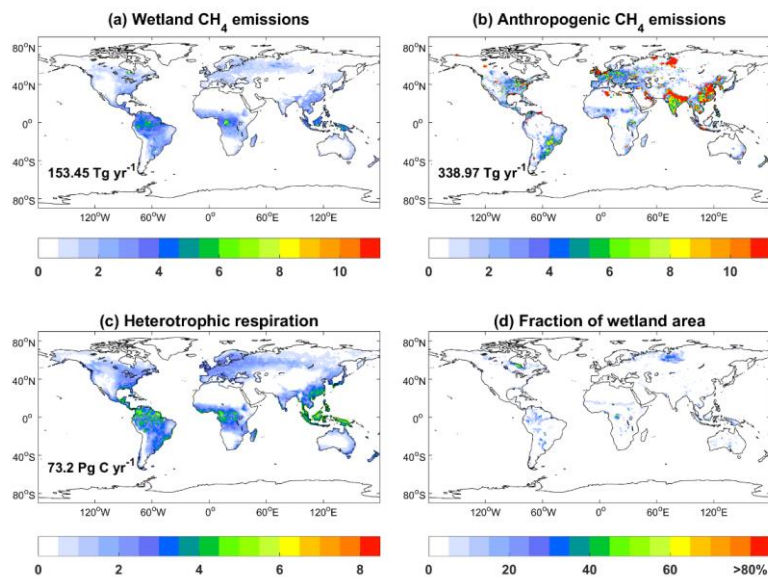
1266

1267

**Figure 8** Absolute ( $\text{g C m}^{-2} \text{ day}^{-1}$ ) and relative (%) differences of global GPP between simulations with (BASE) and without (BASE\_NW) two-way carbon-water coupling processes. Simulation results are averaged for the period of 1980-2020.



1268  
 1269 **Figure 9** Comparisons of global burned fraction (%) and fire-emitted OC emissions ( $10^{-3}$  kg km $^{-1}$   
 1270 yr $^{-1}$ ) between (a, d) simulations and (b, e) observations. Simulations are performed using iMAPLE  
 1271 and observations are from GFED V4.1 fire emissions products. Both simulations from the BASE  
 1272 experiment and observations are averaged for the 1997-2016 period. The global total area burned  
 1273 are shown on (a) and (b), and total OC emissions are shown on (d) and (e). The spatial difference,  
 1274 correlation coefficient (R), and normalized mean biases between simulations and observations  
 1275 are shown on (c) and (f).  
 1276



1277

1278

1279

1280

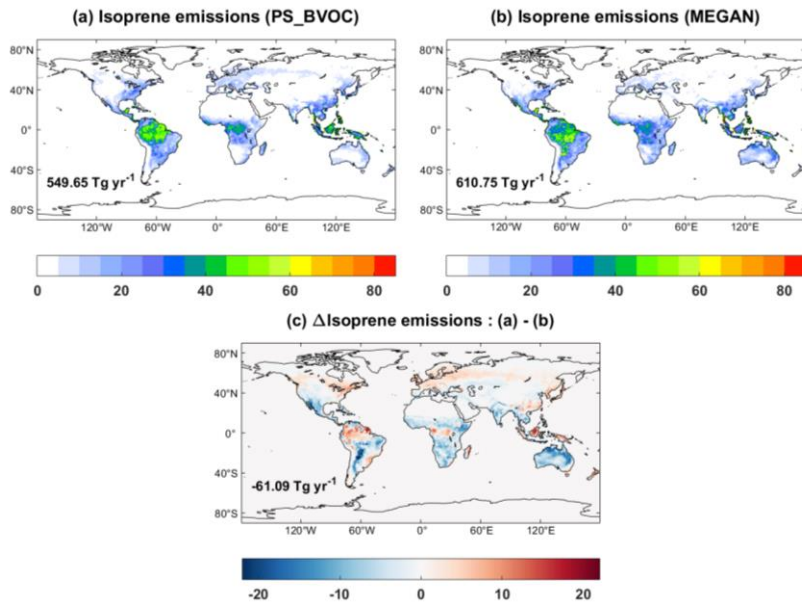
1281

1282

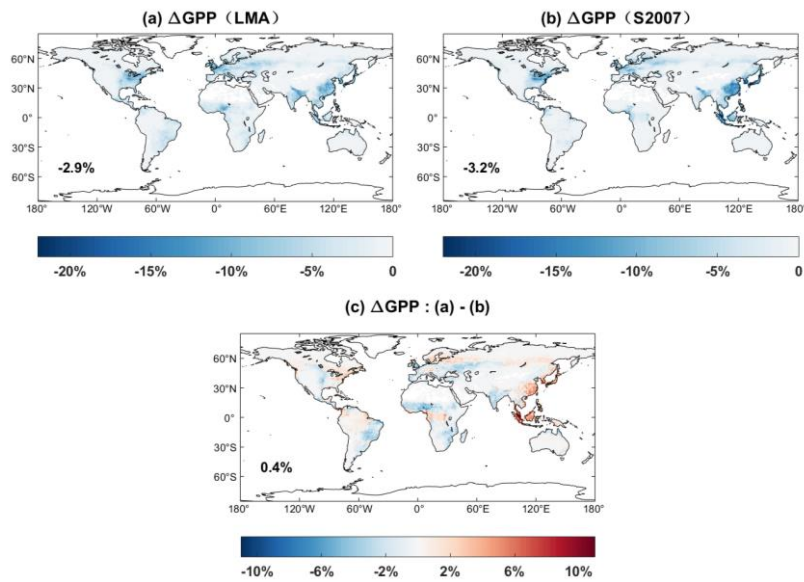
1283

1284

**Figure 10** Global simulated CH<sub>4</sub> emissions (g [CH<sub>4</sub>] m<sup>-2</sup> yr<sup>-1</sup>) from (a) wetland and (b) anthropogenic sources, (c) heterotrophic respiration (gC m<sup>-2</sup> day<sup>-1</sup>) and (d) fraction of wetland area. The simulations are from the BASE experiment. Anthropogenic sources are adopted from CMIP6 including the sectors of energy, agriculture, industrial, residential, shipping, solvent and transportation. The global total emissions and heterotrophic respirations are shown on each panel. All variables are averaged for 2000-2014.



1285  
 1286 **Figure 11** Global isoprene emissions ( $\text{mg C m}^{-2} \text{ day}^{-1}$ ) from (a) MEGAN, (b) PS\_BVOC schemes  
 1287 and (c) their differences during 1980-2020. The simulations are from [the](#) BASE experiment. The  
 1288 global total emissions are shown on each panel.  
 1289



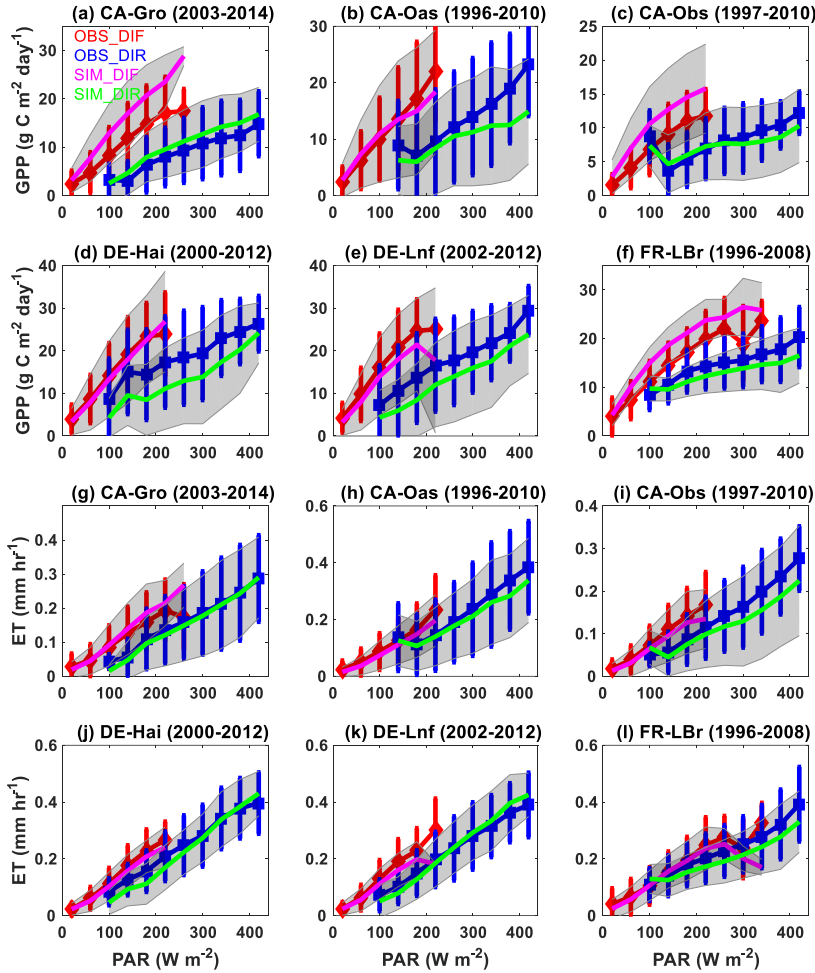
1290

1291 **Figure 12** Percentage changes of global GPP caused by ozone damage effects based on (a) LMA  
 1292 (O3LMA – BASE) and (b) S2007 (O3S2007 – BASE) schemes. The ozone damage schemes  
 1293 include (a) trait leaf mass per area (LMA)-based from [the](#) O3LMA experiment, (b) S2007 plant  
 1294 ozone sensitivity from [the](#) O3S2007 experiment and (c) their differences.

1295

1296

1297



1298  
 1299 **Figure 13** Observed and simulated responses of site-level (a-f) GPP and (g-l) ET to diffuse and  
 1300 direct radiation at the FLUXNET sites. Photosynthetically active radiation (PAR) reaching the  
 1301 surface are divided into diffuse (diffuse fraction > 0.75) and direct (diffuse fraction < 0.25)  
 1302 radiation at six FLUXNET sites with more than 10 years of observations. Observations  
 1303 (simulations) are grouped over PAR bins of 40 W m<sup>-2</sup> with errorbars (shadings) indicating  
 1304 standard deviations of GPP and ET for each bin. The red (blue) and magenta (green) represent  
 1305 observed and simulated responses of GPP and ET to diffuse (direct) radiation. Units of GPP and  
 1306 ET are g C m<sup>-2</sup> day<sup>-1</sup> and mm hr<sup>-1</sup>, respectively.

1307